ABSTRACT

PHASE SPACE DENSITY STUDIES ON
CYCLOTRON ION SOURCES

by Merrit L. Mallory

A facility has been set up for development and testing of cyclotron ion sources with special emphasis on capability for rapid phase space density measurements. H^+ ions from the test source are accelerated into a - 30 kV dc "dee" and magnetically deflected through 180°. A system of remotely adjustable slits is mounted inside the dee and is used to determine the axial and radial emittance areas.

The phase space density has been determined from the axial and radial emittance area measurements at a variety of arc conditions and for a number of source geometries. All studies have employed a 0.062" x 0.375" source output slit with arc currents varied from 1 to 5 amps. Geometrical variations have been principally concerned with source face shapes. Both axial and radial emittance areas from a normal flat source are found to have a considerable admixture of coherent motion which results in inefficient use of the aperture and also, in combination with nonlinear fields, can lead to an effective dilution of the phase space density. Moderate recessing of the source contributes a focusing force in both r and z and makes the phase space volume much more compact.

The effects of plasma boundary and space charge are evidenced in the axial measurements. The axial plasma

boundary is found to be concave, with the result that ions emitted from the top and bottom of the ion source slit focus toward the median plane. Space charge effects are clearly discernable; the axial width of the beam linearly increases as a function of total beam current. In the radial emittance area measurements, an asymmetry in the radial position of maximum current was found and traced to a shifting plasma boundary. This shift was subsequently shown to be the result of a strain displacement of the ion source filament.

PHASE SPACE DENSITY STUDIES ON CYCLOTRON ION SOURCES

By

Merrit Lee Mallory

A THESIS

Submitted to
Michigan State University
in partial fulfillment of the requirements
for the degree of

DOCTOR OF PHILOSOPHY

Department of Physics and Astronomy

1966

ACKNOWLEDGEMENTS

I thank Dr. H. G. Blosser for his suggestion of the research topic and continued guidance. I also thank Dr. M. Reiser for the initial planning and construction of the apparatus.

I am grateful to the National Science Foundation for making this work financially possible.

I am appreciative of the following technical staff who participated in construction of the experimental apparatus: R. Geyer, D. Magistro, and a very special thanks to N. Mercer. I also appreciated the assistance received from T. Arnette, R. Dickenson, D. Johnson and P. Pierson.

I am greatly indebted for the assistance I received from D. Cluxton in apparatus maintenance and data taking, and finally I shall always be grateful to my wife, Barbara, for her typing and continued moral support.

TABLE OF CONTENTS

Page

LIST OF TABLES

LIST OF FIGURES

Page

INTRODUCTION

The most important overall figure of merit of an accelerator is the density of the output beam in phase space. With respect to the accelerator proper high density reduces aperture requirements in both the accelerator and in the associated beam handling systems. For the cyclotron, in particular, provision of adequate aperture through the extraction system is an exceedingly formidable problem—increased density is therefore particularly beneficial in this area. With respect to the functioning of the accelerator as a nuclear physics research tool, the optimum resolution obtainable with a high resolution magnetic analysis system is determined by the phase space density of the accelerator beam[1]. In modern nuclear physics resolution is the primary factor in determining the feasibility and validity of many experiments.

In the absence of space charge interactions the six dimensional phase space volume of an accelerator beam is, from Liouville's theorem, a constant of the motion and the phase space density of the external beam therefore relates linearly to the density of the beam as it leaves the ion source—improvements in the source density are directly reflected in improved density in the external beam. Even when space charge forces are included, the linear relationship between initial and final densities in the six dimensional phase space remains valid for ion densities such that the aggregate of particle-particle forces can be represented

by a potential function[2]. For ion densities typical in accelerator operation, this is an excellent approximation and, therefore, even with space charge effects included improved source density is directly reflected in improved output density.

Very careful and complete measurements of the phase space density of a duoplasmatron ion source[3] and a rf ion source[4] have been made. With respect to a cyclotron ion source, no previous density measurements are available (an estimate of the density was made by Blosser and Gordon[5] on the basis of central region studies in the Canberra cyclotron by W. I. B. Smith[6].) This report presents a description of an ion source testing facility and the results of dc phase space density measurements of a cyclotron ion source for a variety of arc conditions and for a number of different ion source chimney geometries.

Let the coordinates r and z designate displacement at right angles to the principle direction of motion of a beam of particles, and p_r and p_z the corresponding conjugate momenta. The phase space density of some small element of the beam is then the current (particles per unit of time) in the element divided by the product of the spreads in energy, in r, in p_r, in z and in p_z of the element:

$$D = \frac{I}{(\Delta r)(\Delta p_r)(\Delta z)(\Delta p_z)(\Delta E)} \, . \qquad (1)$$

In most accelerators coherent phenomena introduce energy spreads which are large in comparison with the intrinsic energy spread from the source. It is therefore customary to measure a reduced density called the luminosity, L, given by

$$L = \frac{I}{A_r A_z} , \tag{2}$$

where A_r (the radial emittance area) is defined as the product of the radial spread, Δr, and its radial angular divergence α_r ($\alpha_r \simeq \Delta p_r/p$ for small angles) for a given beam current I:

$$A_r(I) = (\Delta r)(\alpha_r) \simeq \frac{(\Delta r)(\Delta p_r)}{p} , \tag{3}$$

where p is the total momentum. Likewise, A_z (the axial emittance area) is defined as the product of the axial spread, Δz, and its axial angular divergence α_z ($\alpha_z \simeq \Delta p_z/p$ for small angles) for a given beam current I:

$$A_z(I) = (\Delta z)(\alpha_z) \simeq \frac{(\Delta z)(\Delta p_z)}{p} . \tag{4}$$

The luminosity is then related to the phase space density by

$$L = D\Delta E p^2 . \tag{5}$$

The problem of determining L can be reduced to measuring A_r and A_z separately for equal current values provided no coupling exists between r, p_r and z, p_z. This is the case encountered in a uniform magnetic field. For this reason, considerable effort was expended to ensure that the cyclotron ion source in the test facility operated in such a field. However, coherent coupling effects may still be present where the coupling has occurred in the ion source plasma or in the region between ion source and puller. These effects can be measured but would require a large amount of time. Hence for the results reported herein, the axial emittance measurements are for all radial portions of the beam (i.e., $-\infty < r < +\infty$) and the radial emittance measurements are for all axial portions of the beam (i.e., $-\infty < z < +\infty$), i.e., coupling effects have been neglected.

The axial emittance area is measured by allowing the ion source beam to illuminate a 0.025" axial slit adjustable over the entire beam height. The extreme positions for which current passes through this slit determines the axial beam spread, Δz. At some point further along the beam trajectory the axial angular divergence, α_z, for each position of the axial aperture is found by measuring the axial beam spread with a differential probe.

The radial emittance areas are measured in a similar manner, except now the angular divergences and radial width

probes are a quarter betatron wavelength apart due to magnetic focusing. Namely, the momentum probe is at the 90° beam position (0° corresponds to beam at ion source) where the maximum radial width occurs for a given initial angular divergence. The radial width probe is at 180° since it is difficult to insert a probe at 0° without causing high voltage and electric field shielding problems.

In this set of experiments, the following parameters were held constant: magnetic field of 4.2 kG; dee power supply voltage setting of - 30 kV dc; ion source arc voltage at - 100 volts, ion source H_2 gas flow of 1.5 cc/min; puller geometry and source position (Sec. 1.7). The parameters changed were the source geometry and the arc current.

I. EXPERIMENTAL APPARATUS

1.1 Introduction

The ion source testing facility apparatus may be thought of as a "one-turn" cyclotron. Namely, the apparatus consists of (1) a magnet, (2) a vacuum system, (3) an ion source (a copy of the MSU cyclotron ion source), (4) a dc "dee" to provide the one-turn acceleration and (5) various slits and probes to make measurements. A picture of the ion source testing facility is shown in Fig. 1. The magnet is located in the center, while to the left of the magnet is the current probes metering cage. Below the metering cage are the vacuum controls and gauges. The dee voltage supply is enclosed in the fenced area and its controls are in front. To the right of the magnet are the various ion source power supplies. The magnetic field controls, installed to the far right, are not shown. These components are described in more detail in the following sections.

1.2 Magnet

1.2.1 Magnet Yoke

Figure 2 is a cut-away drawing of the assembled magnet showing the overall dimensions. The typical H-type magnet was constructed from SAE #1010 steel. The pole diameter is

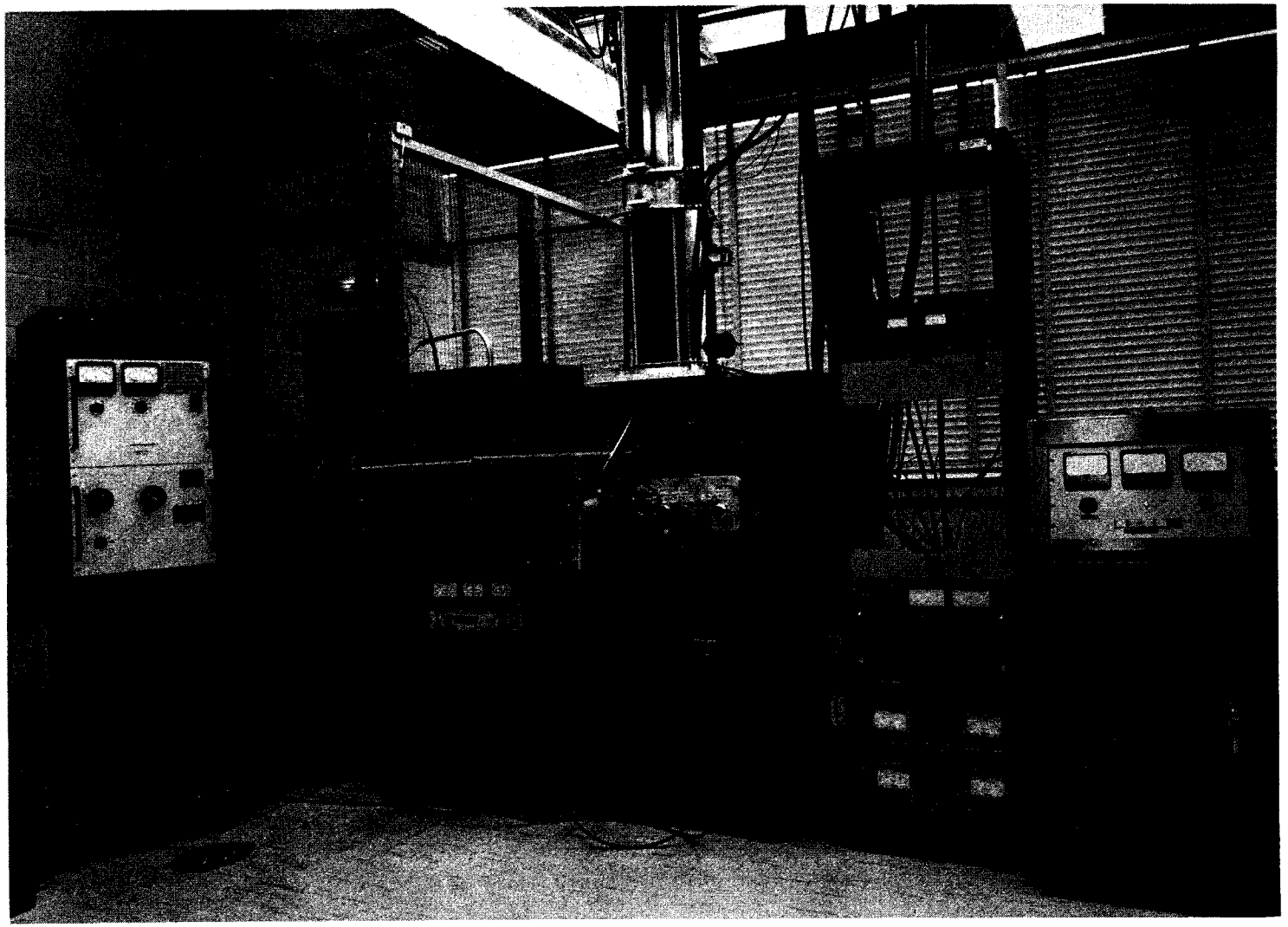

Fig. 1: View of ion source testing facility. The magnet is located in the center, while to the left is the high voltage metering cage. Below the metering cage are the vacuum controls and gauges. The dee voltage power supply is enclosed in the fenced area and its controls are in front. The various ion source power supplies are lodged at the right of the magnet. The magnet field controls, installed far right, are not shown.

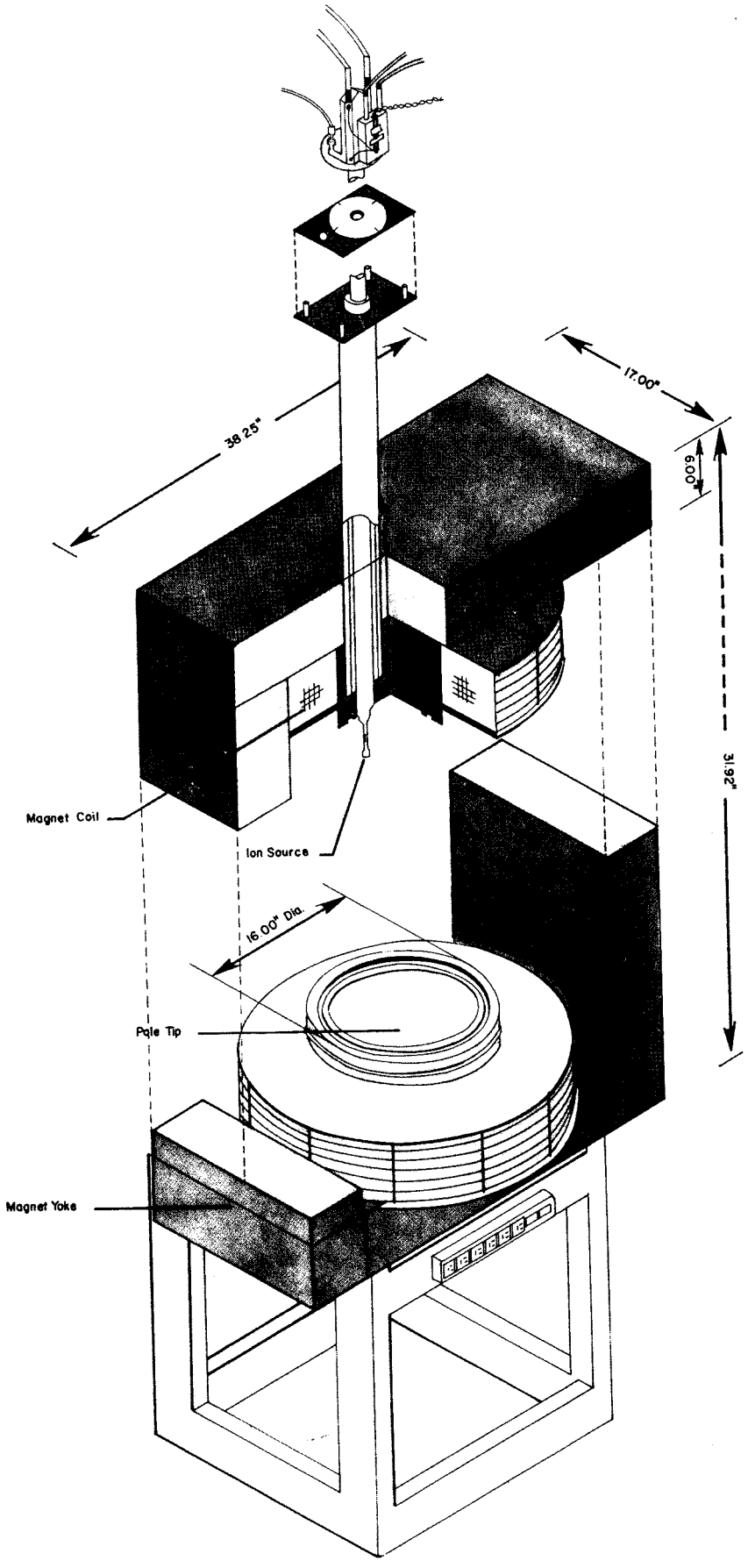

Fig. 2: Cut-away drawing of ion source magnet. The important dimensions of the magnet are given in the figure. The ion source (top of figure) is inserted axially into the magnet gap.

16", the magnet gap varying from 4" at the magnet center to 3.6" on the shim rings.

1.2.2 Magnet Coils

The magnet coils are also illustrated in Fig. 2. Each coil consists of six subassemblies called "pancakes". The pancakes are double-layered coils, each layer having twelve turns of square copper tubing (0.438" x 0.438" outside, 0.313" inside diameter). Overall dimensions of a pancake are as follows: inside diameter, 16.06"; radial width, 6.03"; height, 0.936". The pancake, fabricated from two 70 foot long strands of tubing (the longest length available), has a brazed joint located on the I.D. of the pancake at the transition between layers. Turn-to-turn insulation consists of a manually wrapped, single layer of an epoxy loaded glass tape*. In addition an external epoxy coating was applied to each pancake for added mechanical strength. The pancakes were tested for turn-to-turn electrical shorts by inserting a needle probe into contact with each turn and measuring the corresponding voltage drop with a coil excitation of 200 amps.

1.2.3 Magnet Power Supply

The magnet power supply is a 50 kW motor generator and regulator. A chopper in the regulator samples the shunt

---

* Minnesota, Mining and Manufacturing Company, Scotchply 1010, 1/2" width.

voltage of the generator output and an adjustable reference voltage producing a 60 cps square wave with amplitude proportional to the voltage difference. This signal is amplified and added to a phase shifted ac signal. The combined signals are applied to the grids of a pair of thyratrons, where the firing angles of the thyratrons are shifted from 90 electrical degrees depending on the sign and magnitude of the square wave. The thyratrons control the magnetic field of the generator resulting in regulation of the supply.

Originally the magnet regulator unit was very noisy and led to interference with other electronic equipment throughout the building. Adding a choke to each leg of the input power line and adding a pi filter to the plates of the thyratrons greatly reduced the noise. The regulation of the power supply was checked by inserting a nuclear magnetic resonance probe between the pole tips and measuring the magnetic field drift. The 9 kG field was found to be stable to $\pm$ 4 gauss.

Two types of trouble have occurred with the power supply. The most common one occurs when thyratrons go bad; large oscillations in the regulator produce large magnetic field variations. The second problem occurs when the chopper wears and becomes noisy; large noise-type magnetic field variations resulted.

1.2.4 Magnet Pole Tips

Two sets of pole tips were designed for the magnet, one for field values of 4 to 7 kG and the other for field values

of 10 to 12 kG. The design goal was to make the field uniform for as large a radius as possible. The definition of "uniform" used is that ν_z be less than 0.05 where

$$\nu_z^2 = - \frac{dB/B}{dr/r} . \qquad (6)$$

In this relation, r is the radius at which B (the magnetic field) is measured and dB is the change in the magnetic field for a given change in the radius dr. Another requirement was that the main magnet gap be 4" at the center of the magnet.

The process of designing the pole tip was empirical. The magnetic field was first measured on the magnet measuring facility[7] with a flat pole tip and a central magnet gap of 3.250". A small cylindrical section was machined from the pole tips and the magnetic field again measured. The two measurements, normalized at the central magnetic field, were subtracted, giving the change in magnetic field for a given change in pole-tip configuration. The decision on the next machining operation on the pole tips was made from the above information. A series of fifteen machining operations determined the design of the low field pole tips. The magnetic field measurements of the low field pole tips at the high field excitation were used to design the high field pole tips. Only six machining operations were needed on the high field pole tips. Figures 3 and 4 give a cross section of low and high field pole tips and their corresponding magnetic fields as a function of radius.

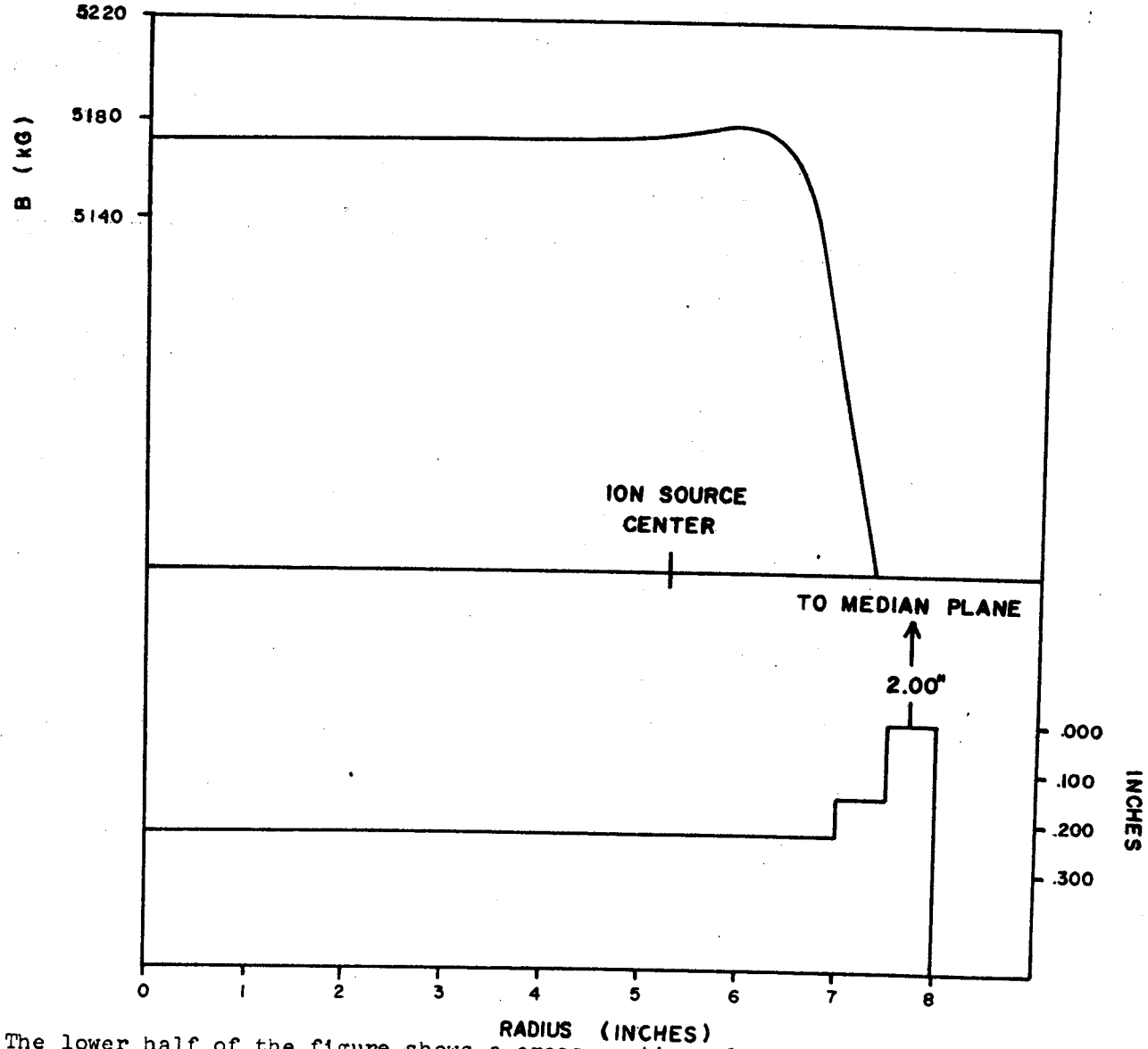

Fig. 3: The lower half of the figure shows a cross section of the low magnetic field pole tip. The upper half of the figure is the magnetic field B (kG) versus pole tip radius. The magnet center is 0.000".

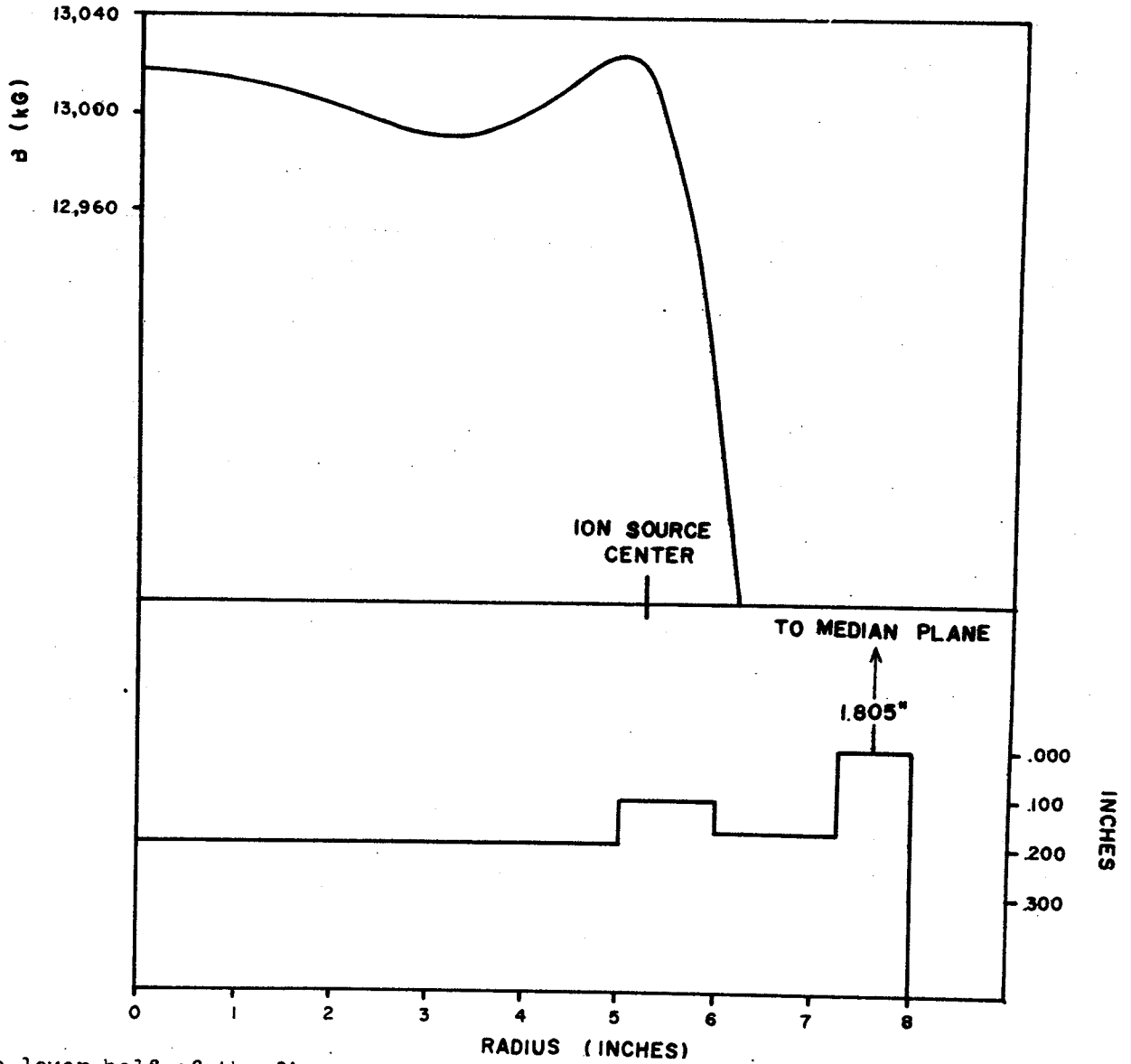

Fig. 4: The lower half of the figure shows a cross section of the high magnetic field pole tip. The upper half of the figure is the magnetic field B (kG) versus pole tip radius. The magnet center is 0.000".

1.2.5 Ion Source Magnet Hole

The hole in the magnet yoke for insertion of the axial source was determined from the magnetic field measurements. The hole was located 5.345" from the magnet center. This distance was determined by the magnetic field fall-off of the high field pole tips. The source hole was also displaced 1" to the left of the magnet center line with respect to the yoke (see Fig. 2). This positioning allowed the puller to be aligned on the center line of the magnet. A 2.875" diameter hole was drilled and bored at this location through the upper yoke, upper pole root, lower yoke and lower pole root. Pole tips were installed on the magnet and the center of the bored hole transferred to them. A 1.500" diameter hole was bored in the top pole tip.

The magnetic field in the median plane of the magnet was measured to determine the effect due to the loss of iron in the ion source hole. Figure 5 shows the percent change in the measurement of the median plane magnetic field with the probe located 1" to the left of the magnet's center line as compared to a measurement of the field 1" to the right of the magnet's center line. The change in magnetic field was so small that ion source hole shimming was not warranted. The net change in magnetic field is even less than measured since magnet steel was used where possible in the construction of the lower 1/3 of the ion source.

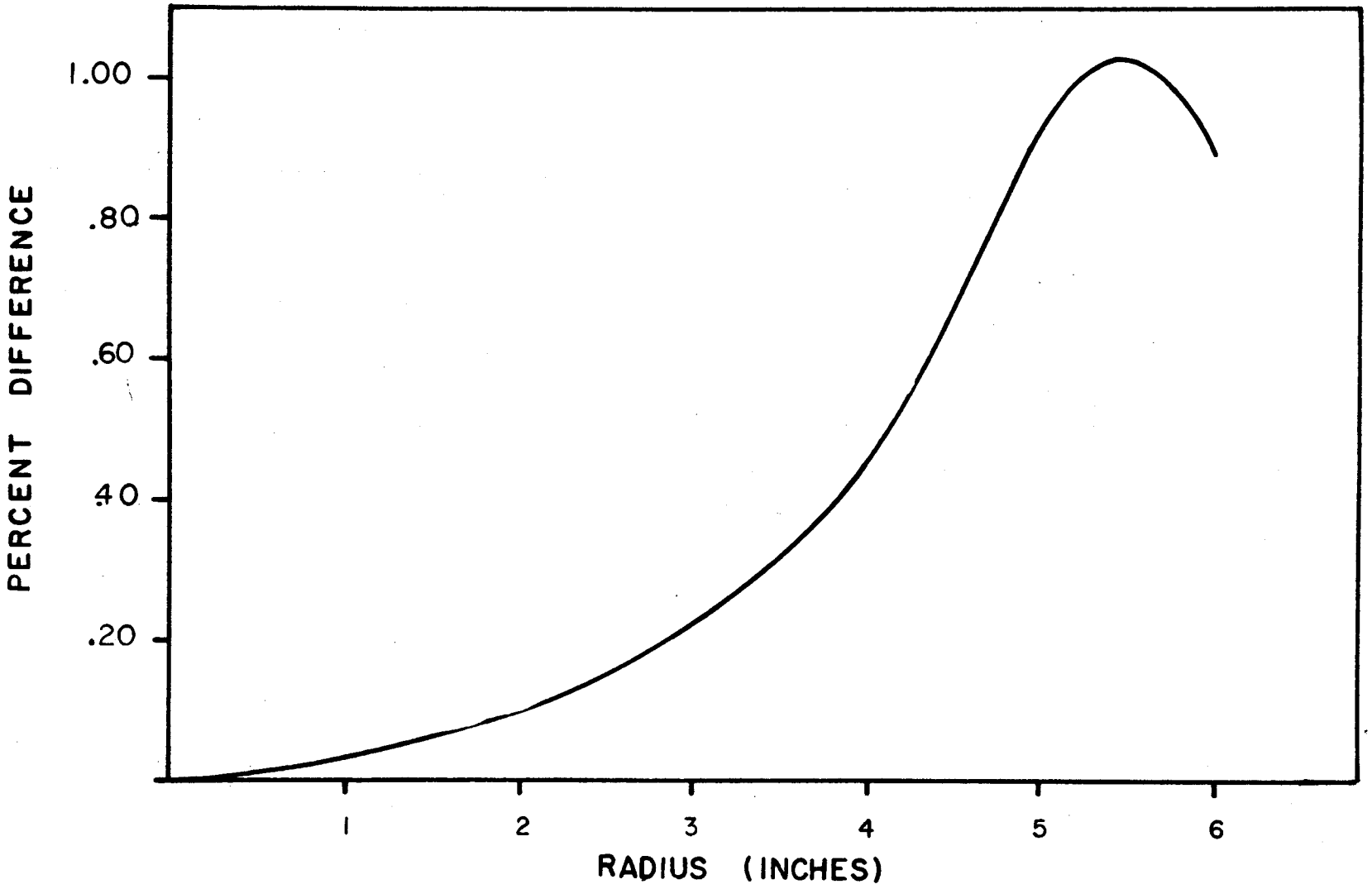

Fig. 5: The percent difference in the median plane magnetic field between measurements with ion source hole and no ion source hole in the pole tip. The net percent difference is expected to be less than the measured value, since the bottom third of the ion source is constructed, where possible, of magnet steel.

1.2.6 Magnetic Field Calibration

For the calibration of the magnetic field a nuclear magnetic resonance (NMR) probe was used. This was centered exactly by adjusting the probe position for a maximum field value. The frequency of the NMR probe was measured as a function of magnet current (measured with a Rubicon potentiometer across a 100 mV-800 amp shunt). Figure 6 shows the calibration curve of the central field in kG versus shunt potential (mV). Hysteresis effects were minimized to $\pm$ 1 gauss by following the procedure of turning the power supply up to maximum current, turning it off, and finally turning the power supply up to the desired current.

1.3 Vacuum System

1.3.1 Main Vacuum Chamber

A cut-away drawing of the main vacuum chamber is found in Fig. 7. The chamber sides are made from 1" thick aluminum heliarced together. The ends of the vacuum chamber are removeable to provide easy access to the chamber. The pole tips shown at the front of the main chamber are gasketed to the chamber walls. The diffusion pump is attached at the back of the chamber and situated directly above it is the main vacuum valve. Various ports in the chamber walls permit viewing and insertion of probes.

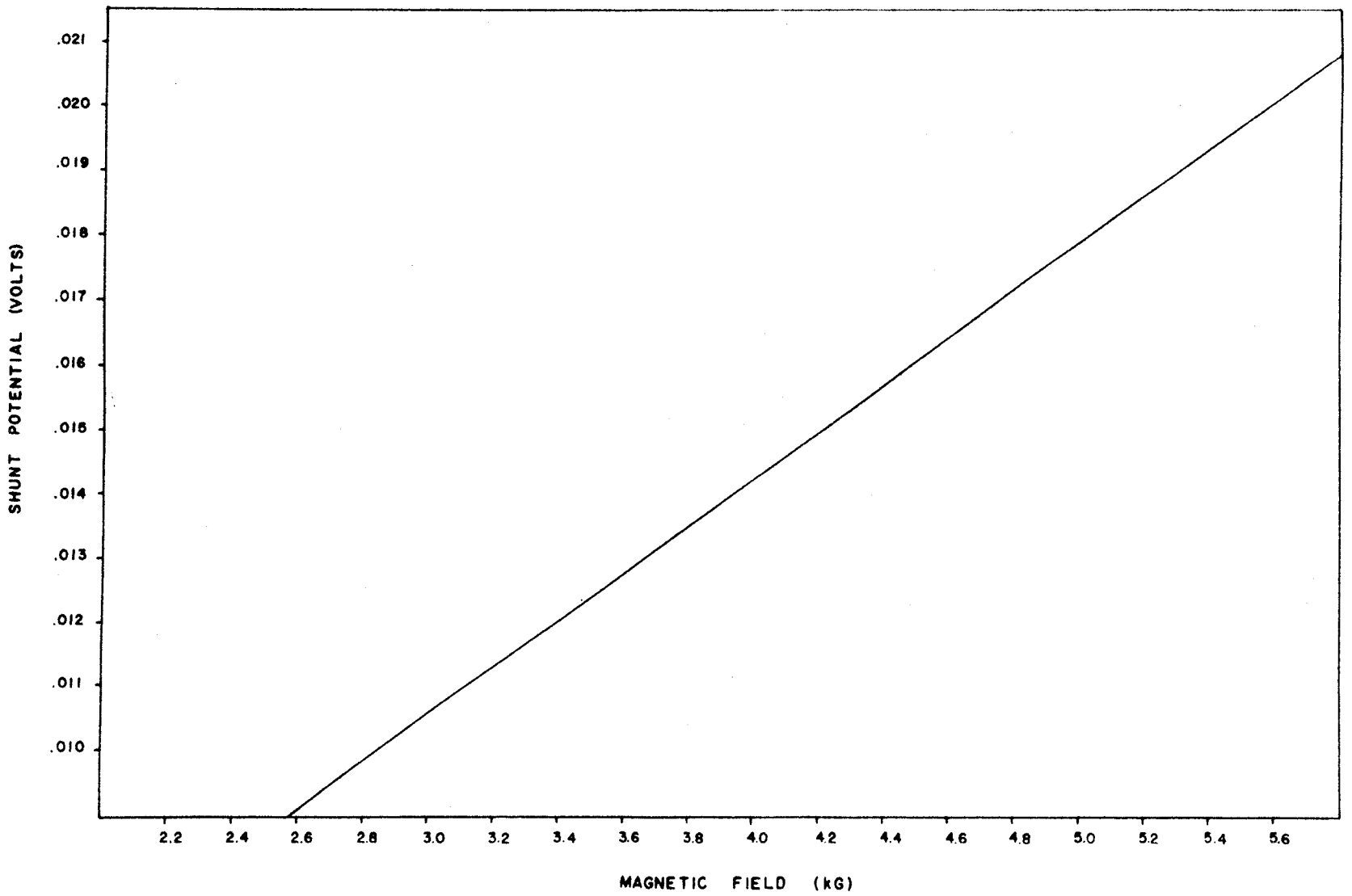

Fig. 6: Central magnetic field versus coil excitation. The magnetic field was measured with a nuclear magnetic resonance probe. The coil excitation is determined by measuring the potential across a 100 mV-800 amp shunt. The hysteresis effect could be neglected when the magnet power supply was turned on in a consistent manner.

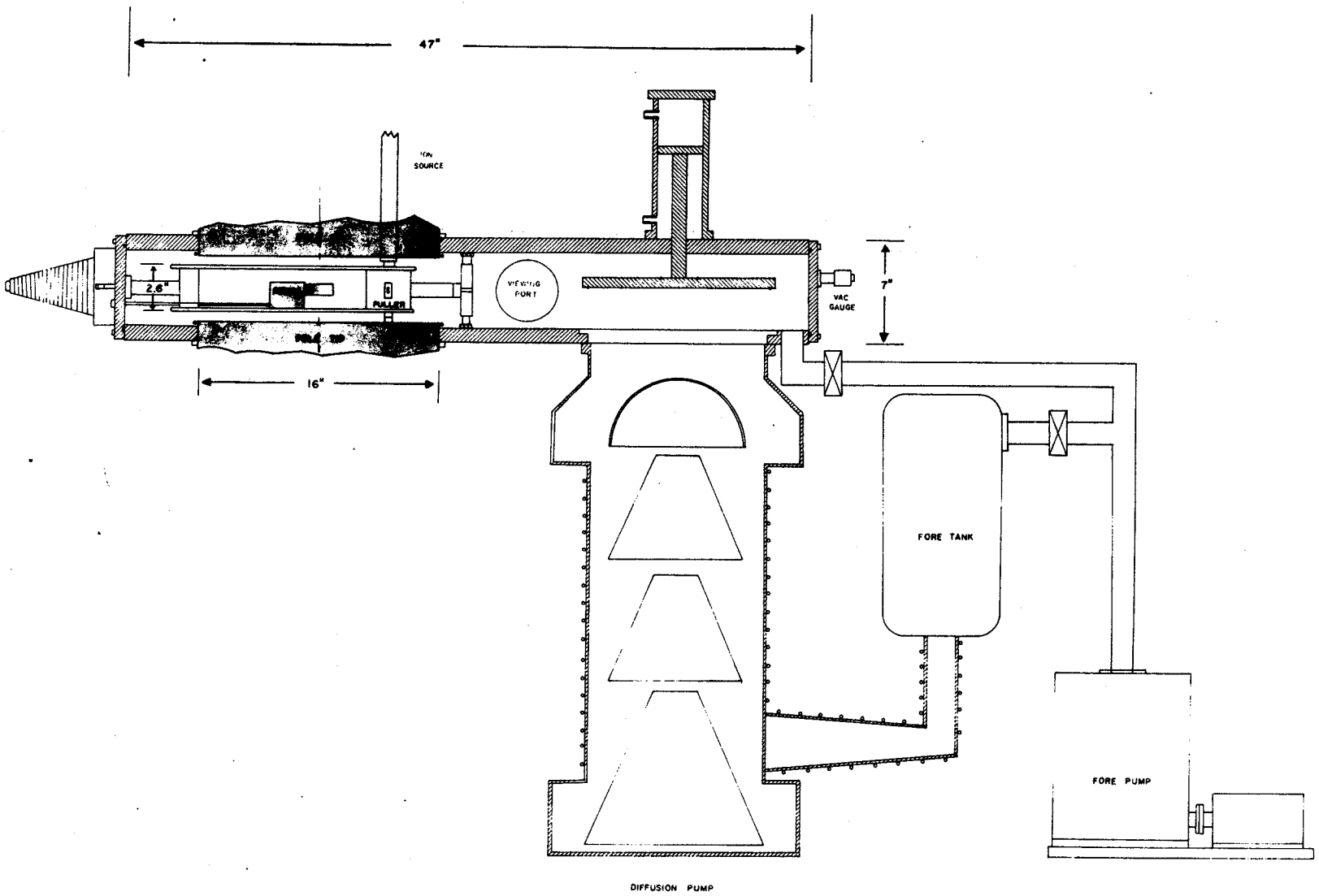

Fig. 7: A cut-away drawing of vacuum chamber. Some of the important dimensions are given. The dee placement between the pole tips is shown.

1.3.2 Mechanical Vacuum Pump

The mechanical vacuum pump, a Consolidated Vacuum Corporation E-70A rotary pump, has a pumping speed of 41 CFM. The pump down time for the entire vacuum system to 50 microns is 5 minutes. The pump is encased in an insulated wooded housing to reduce pump noise.

1.3.3 Diffusion Vacuum Pump

The diffusion vacuum pump* (using Narcoil-40 oil) has a pumping speed of 8900 CFM at 0.1 micron and typical pump-down time from 50 microns to 2×10^{-5} mm of Hg is 15 minutes. Such a short pump-down time makes it quite convenient to make frequent changes inside the main chamber. The diffusion pump oil is protected by an upper limit vacuum switch on a Philips gauge (initially bypassed on pump down). This switch closes the main vacuum valve when tripped.

1.4 Cyclotron Ion Source

1.4.1 Ion Source Operation

The following is a short description of the operation of a cyclotron ion source. The filament of an ion source is heated to high temperature and produces thermal electrons. A potential of ~ 100 volts between the filament and the

---

* HS 10-4200 Purifying Diffusion Pump Type 163, NRC Equipment Corporation.

chimney (arc voltage) accelerates the electrons. The electrons are in a strong axial magnetic field and hence travel in helical trajectories along the field lines to the bottom of the chimney. At the chimney bottom is located an electrically insulated tantalum button. The button builds up a negative charge and hence repels the electrons back up the chimney. To produce H^+ ions, Hydrogen gas is allowed to randomly flow into the chimney. Hydrogen gas that collides with an electron is disassociated and ionized. Once an arc is struck, i.e., the Hydrogen ionized, the ions form a plasma.

The disassembled ion source (MSU Drawing Number DA-112-100-H) is shown in Fig. 8. The ion source is composed of two main subassemblies: the outer steel jacket and the inner filament leads. The top of the ion source (Fig. 2) contains the manifold for the connection of the water, electricity and gas.

1.4.1.1 Outer Jacket. The ion source outer steel jacket serves many functions. It furnishes a mount for the chimney, contains the filament leads, provides cooling and is an entrance for the gas flow. The length of the outer jacket from the bottom of the manifold to chimney mount is 33.20"; the outer diameter is 1.375". The upper 2/3 of the outer jacket is constructed of steel tubing. The bottom 1/3, constructed of solid steel, has a central hole for the filament leads assembly and rifle-drilled holes for the gas and cooling water tubes. This design was used to minimize the iron loss in the pole tip at the source hole. Each water line in

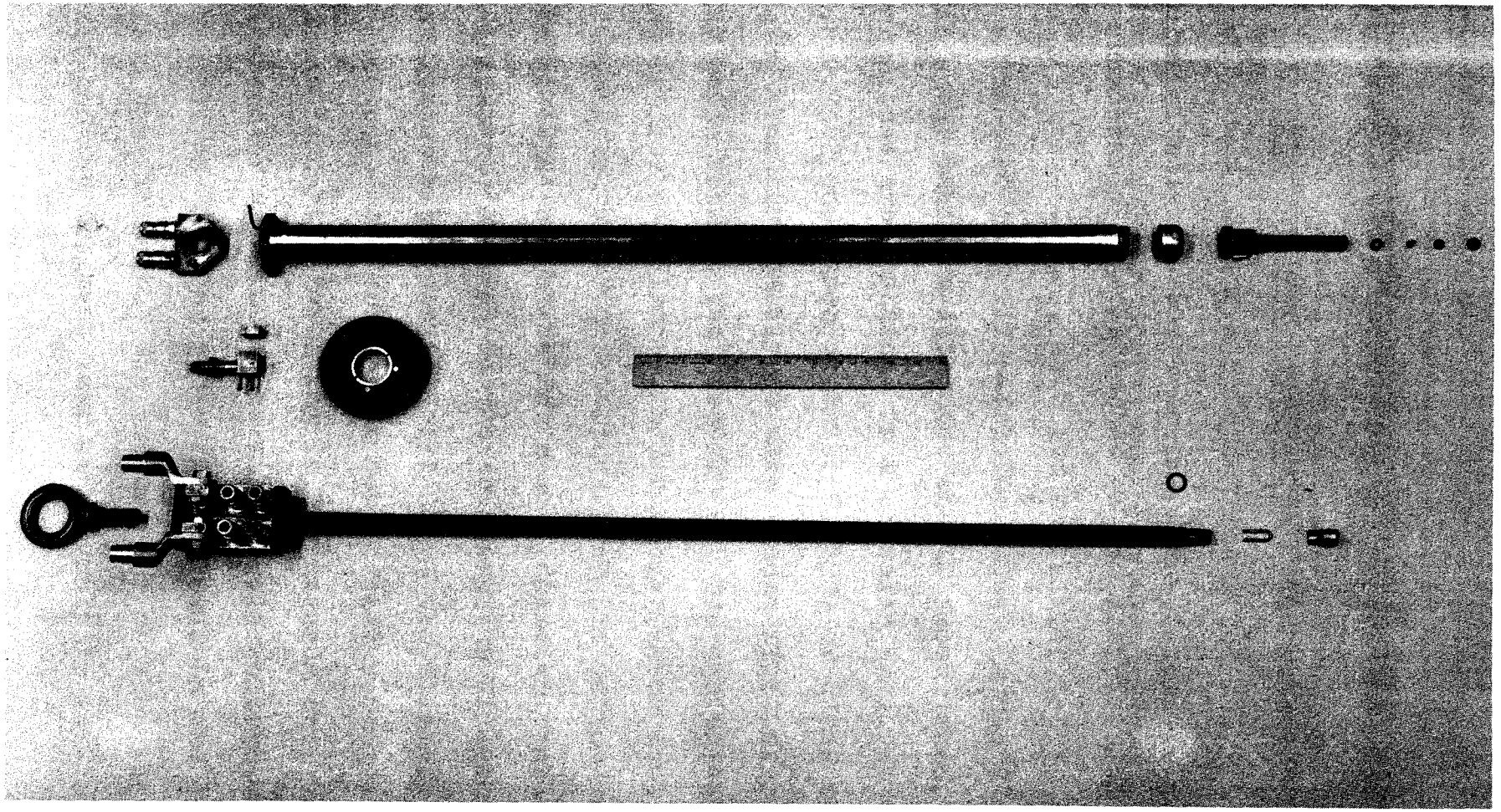

Fig. 8: Picture of disassembled ion source. Top (left to right): outer jacket, chimney housing, chimney and reflector button assembly. Bottom (left to right): filament lead subassembly, filament and filament heat shield.

the outer jacket is one continuous piece of 1/8" copper tubing. This type of construction insured that no internal water leaks would occur within the vacuum system.

1.4.1.2 Filament Lead Subassembly. The filament lead subassembly supplies the electrical leads for the filament and is electrically connected to one side of the arc voltage. The subassembly is constructed of two semicircular steel rods (filament leads), each rod containing copper cooling tubes inserted into rifle-drilled holes. A 0.062" piece of glass epoxy laminate separates the filament leads. These three pieces are contained in a circular tube (outer diameter 0.750" and inner diameter 0.625") of glass epoxy laminate. The subassembly is made vacuum tight by pouring an epoxy resin between the pieces. The top end of the filament leads are silver soldered into a copper block containing the electrical and water connections. At the bottom end of the filament leads are holes for a 1/8" diameter tantalum hairpin (filament) and set screws to clamp the filament. The epoxy laminate is removed 1 1/2" from the filament end of the assembly. Any epoxy left behind will vaporize when the filament is heated resulting in an unstable arc. Another indication of vaporizing epoxy is a gold coloration of the filament. An "O" ring groove is machined in the epoxy at 2" from the filament. The vacuum seal between the outer jacket and the filament lead subassembly is located at this position.

1.4.1.3 Chimney. The chimney contains the plasma, determines the direction of the beam and provides initial focusing. The chimney is usually made of graphite. Figure 9 gives some of the more important chimney dimensions. The chimney slit length and width was maintained at 0.375" and 0.062", respectively, for all experiments reported herein. The base of the chimney is keyed and lines up with corresponding keys on the outer jacket. The direction of the chimney slit is indicated by a dial plate mounted on the outer jacket at the top of the source. A tantalum "reflector" button, located in the bottom end of the chimney, is electrically insulated from the chimney by a piece of quartz. Grounding the tantalum button causes a reduction in current output.

1.4.2 Filament Power Supply

The filament power supply is a 300 amp, 5 volt power supply with current sensing regulation. The power supply connects to the ion source through electrical quick-disconnects and is usually operated at 240 amps. Meter readings for a filament burn-out are 0 amps and 5 volts.

1.4.3 Arc Power Supply

The arc power supply is a current regulated, voltage regulated supply of 8 amps, 300 volts. The arc supply is usually operated in current regulation, a typical value being 4 amps, at 150 volts. Shorts between the filament leads and

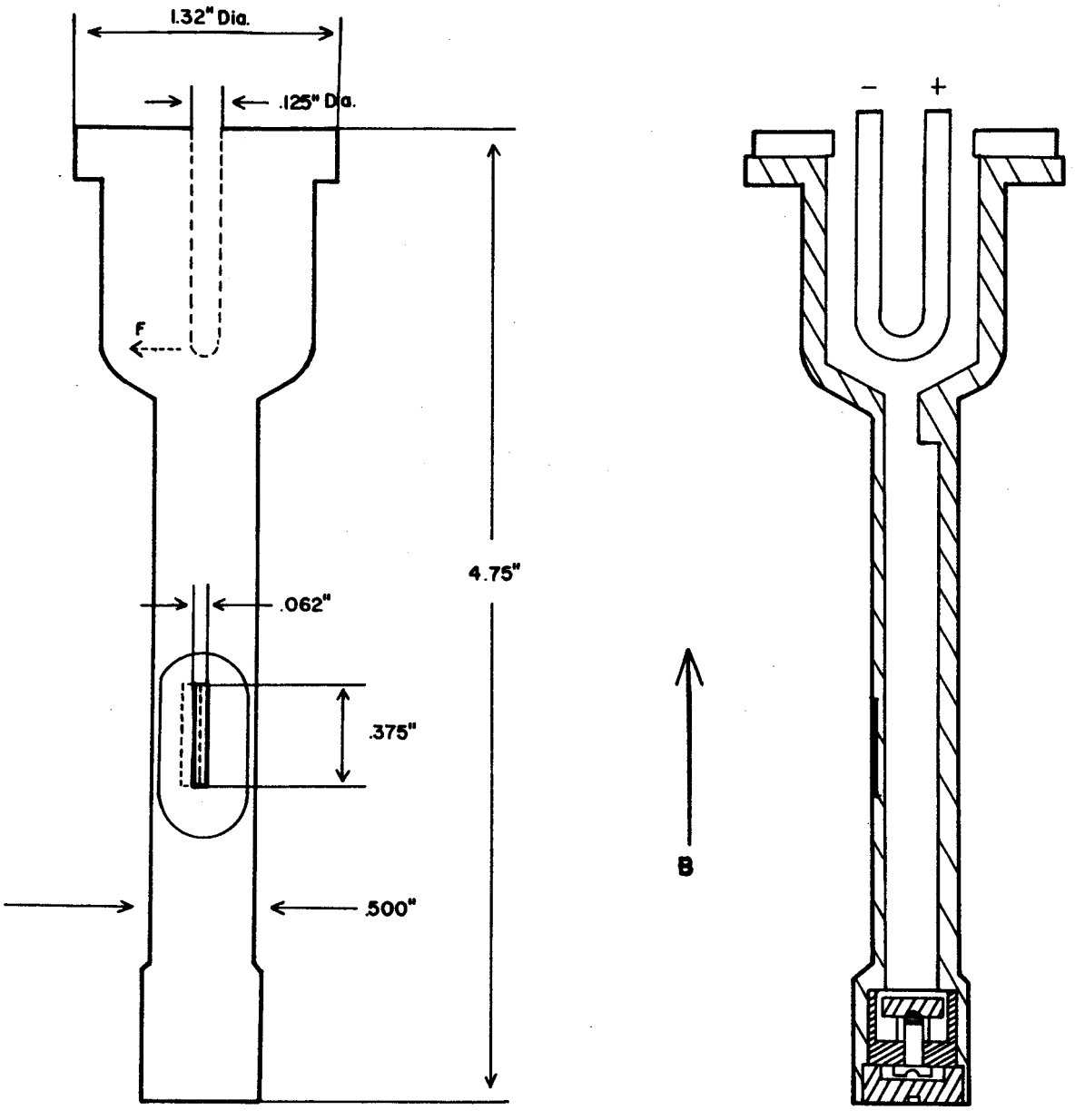

Fig. 9: Drawing of chimney and filament. The dotted chimney slit is the position of the slit in the radial asymmetry experiment. F indicates the direction of the strain force on the filament due to the interaction of magnetic field, B, and filament current.

outer jacket are indicated by a significantly larger current reading for a small voltage.

1.4.4 Ion Source Gas Supply

The ion source gas flow, controlled by a Leybold needle valve, is monitored by a Hastings-Raydist mass flow meter. The gas line is connected to the ion source by a standard LRL-type vacuum fitting. For protons Hydrogen gas of 99.99% purity is used. Gas impurities normally result in a very unstable arc. Typical gas flows for H^+ are 1 to 3 standard cc per minute.

1.4.5 Ion Source Turn-on Procedure

The following are the procedures for turning on the ion source. The arc power supply is set to regulate at the desired current (1 to 5 amps) and voltage (150 volts). The gas flow is set at 2 to 3 cc/min. The filament supply is increased until the desired arc current is obtained.

1.5 Dee

1.5.1 Design and Construction

The lower half of the dee is depicted in Fig. 10. The placement of the dee in the vacuum chamber is shown in Fig. 7. The dee is constructed from two copper plates 3/8" thick x 16" square. The axial height of the dee is 2.6". The dee is mounted on an end plate of the vacuum chamber by means of two hollow ceramic insulators. A third insulator, provided

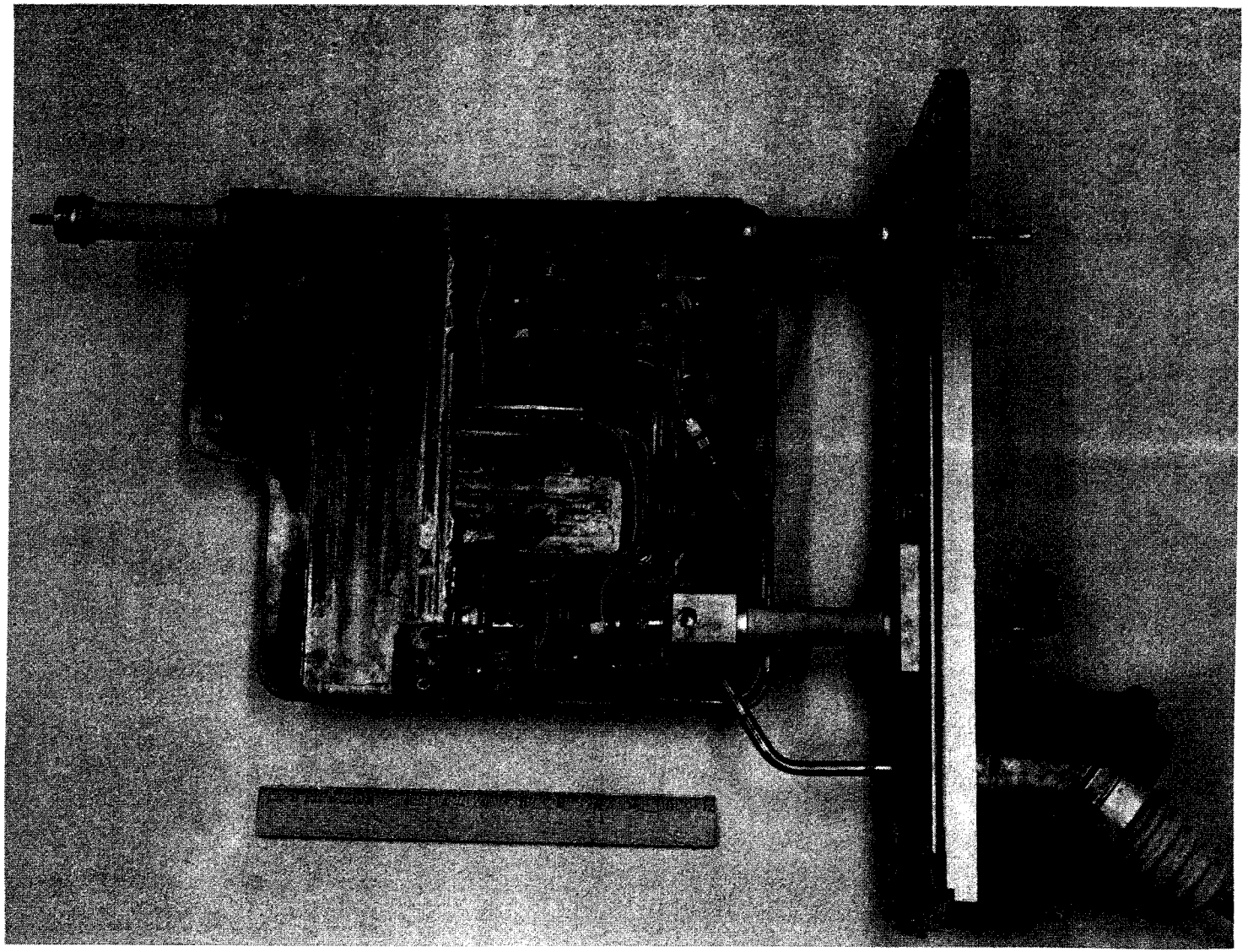

Fig. 10: View of ion source testing facility "dee" with top plate removed. The ion source and puller are located at the indentation on the left side of the dee. The high voltage insulator is at lower right. Water connection for various probes are visible.

on the opposite side, is mounted on a jack to allow some adjustment of the dee height.

The high voltage is fed through a standard power line insulator, consisting of twelve #20 wires inserted through a 3/8" copper tube filled with epoxy. The twelve wires terminate inside the vacuum chamber at a terminal strip and are connected to various probes. Water, to cool the dee and probes, is fed through the insulators to a manifold.

Dee voltage arcing problems were reduced by rounding the dee edges to 3/16" and mirror polishing the outer dee surface. Also it was necessary to install high voltage shields (water cooled) above and below the dee on the pole tips of the magnet. Two additional arcing problems were encountered that required changes. Arcing occurred across the dee ceramic insulators to the vacuum chamber end plate, which was corrected by the installation of corona rings around the insulators. The second problem occurred when accelerating a beam into the dee. The beam would come out from between the dee plates and cause arcing. This was remedied by installing a copper shield wall around the dee edge.

1.5.2 Puller

The puller, an extension of the dee in front of the chimney, is mounted on the bottom plate of the dee by means of a cross slide. The height of the puller is 2" and its width is 2 1/2". The beam slit, centered in the puller, is

1" x 0.325". The radial distance of the puller slit from the ion source chimney can be varied from 0.200" to 0.400" and the lateral position by ± 0.200" from the center of the ion source chimney slit.

1.6 Dee Power Supply

1.6.1 Dee Power Supply Operation and Troubleshooting

The dee power supply voltage can be varied from ± 1 kV to ± 60 kV (in steps of 100 volts) and the current from 0 to 200 mA. Figure 11 shows a block diagram of the supply. The control unit of the supply contains various interlocks and relays. The regulation circuits and the adjustable injection transformer (voltage settings) are in the control unit. The high voltage unit is composed mainly of the high voltage transformer and diode rectifier. The feedback amplifier, which detects the high voltage output through a resistive chain, regulates the high voltage by controlling the grid of the pass tube. The crowbar unit is the dee arc protection. Any arcing that occurs on the dee triggers a thyratron which breaks down a spark gap, allowing the current to arc to ground through the gap. At the same time a relay throws which turns off the high voltage.

The following describes briefly the troubleshooting procedures that can be used when problems are encountered with the dee voltage supply. The tests are done in the following sequence until the problem is corrected:

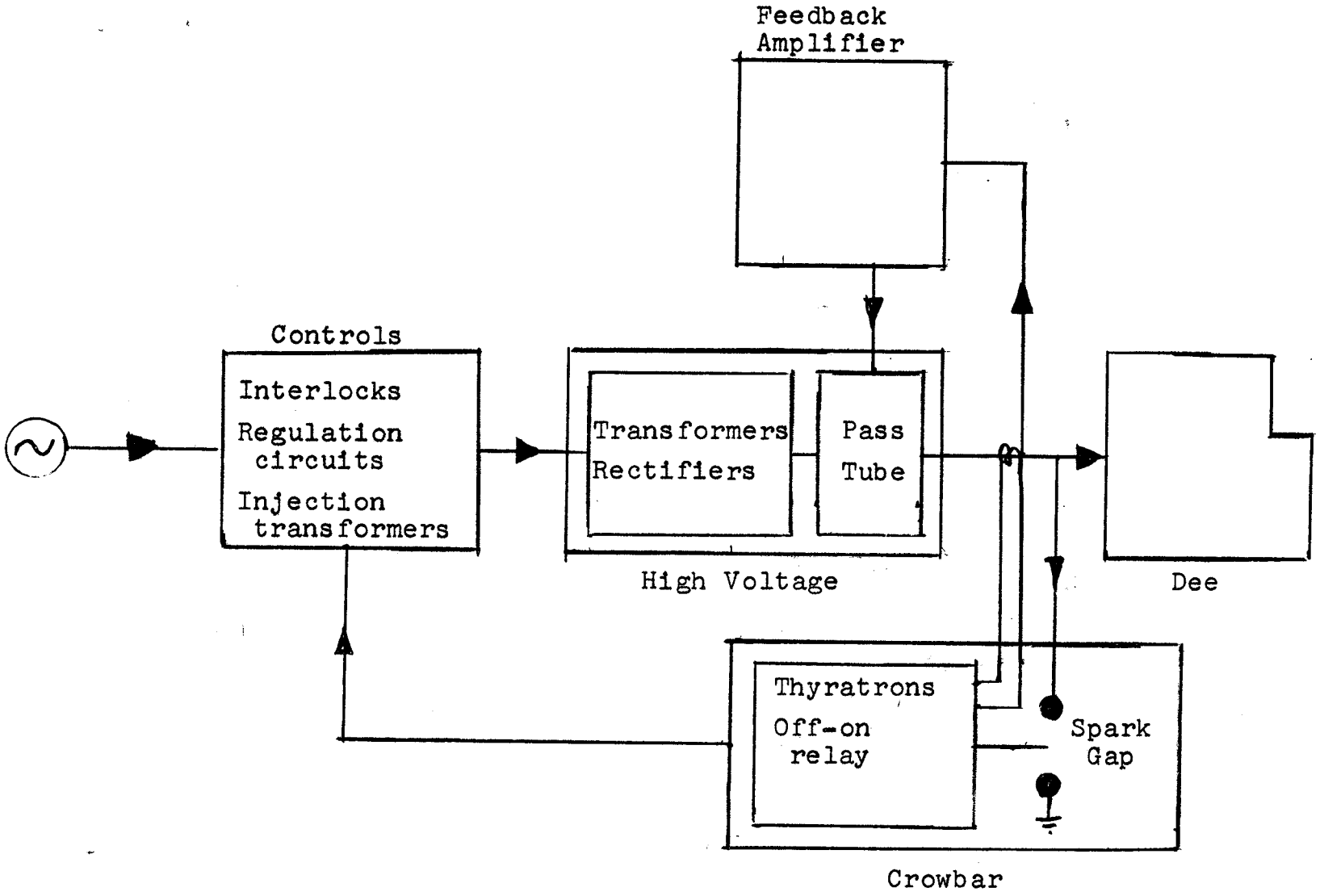

Fig. 11: Dee Power Supply Block Diagram. The power supply is easily divided into four sections: control, high voltage, feedback amplifier and crowbar. Some of the components of each section are listed in the above blocks.

(1) High voltage troubles are checked by listening for hissing sounds that are the results of arcing.

(2) Next bypass the crowbar unit by disconnecting the high voltage from the spark gap. If the unit operates normally, the problem is with the arc sensing thyratron or the high voltage on-off relay.

(3) The control unit is next disconnected from the high voltage transformer and tested by going through the turn-on sequence. The main troubles were bad relays.

(4) The control unit is reconnected to the high voltage transformer and a milliamp meter inserted in the grid of the pass tube of the feedback amplifier. The current in the grid circuit, for proper operation of the amplifier, is 1 mA. The troubles were bad voltage regulation tubes.

Initially high voltage arcing problems were encountered when the ion source was turned on. This turning-on procedure would immediately put a variable load on the dee. The very high gain amplifier would then over-correct for the load, causing the high voltage to oscillate. The crowbar, sensing this oscillation, would turn the unit off. By damping the amplifier response the problem was corrected.

1.6.2 Dee Power Supply Calibration Measurements

A precision resistive chain was connected to the dee voltage line and the potential across the last resistor to ground was measured with a Rubicon potentiometer. The results of the measurement at the power supply setting of 30 kV, as a function of arc current, are contained in Table I.

Table I: The dee voltage measured with a precision resistive chain as a function of arc current. The power supply settings are for 30 kV. The power supply load current is a function of arc current.

Arc Current (Amps)	Dee Voltage (kV)
0.25	29.04
0.50	28.87
1.05	28.83
2.00	28.65
3.00	28.20
4.00	28.20
5.00	27.90

A capacitor, constructed and inserted close to the dee, was used to check the ripple voltage. A 60 cps voltage was applied to the dee and the voltage pickup (in an R-C circuit) was observed with an oscilloscope. Figure 12 gives the 60 cps voltage versus peak-to-peak oscilloscope voltage. The ripple amplitude of the dee power supply was detected with the oscilloscope and found to be 30 volts at 30 kV with a frequency of approximately 360 cps. Turning on the ion source resulted in a ripple voltage of 80 volts at a frequency of ~ 1 kc/sec. However, due to the frequency dependence of the R-C circuit, the amplitude of the ripple is less than 80 volts.

1.7 Probes

1.7.1 Axial Emittance Area Probes

Two probes are needed to measure the axial emittance area and this measuring process is described in Sec. 2.1. The first probe, located behind the puller, is a water cooled horizontal slit (0° slit) which is 0.025" wide. The 0° slit is made of two pieces of 1/8" tantalum clamped to a vertical moving probe which is adjustable over the full beam height. The slit knob is geared to a counter, and the vertical position is determined to $\pm$ 0.005". The second probe is located at the 180° beam position and is a differential current probe. The current probe is a 0.031" diameter tantalum

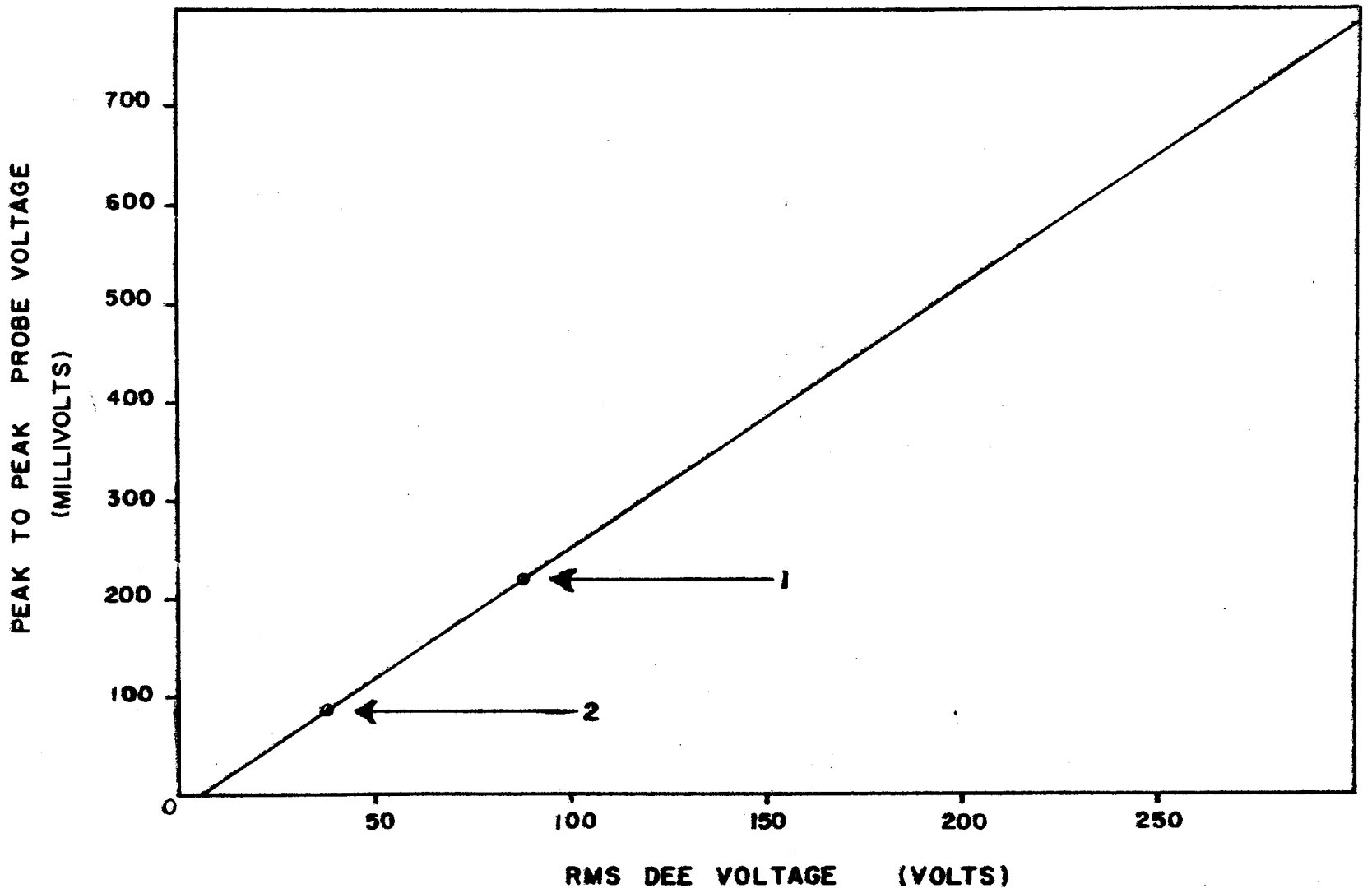

Fig. 12: Ripple voltage measurement of dee power supply. The straight line was determined by applying a 60 cps of known voltage to the dee and observing the peak-to-peak signal in an R-C circuit with an oscilloscope. Points 1 and 2 are values obtained at 30 kV with and without ion source on.

wire, the vertical position remotely adjustable. A counter is attached to the probe and its position determined to $\pm$ 0.005". Figure 13 shows the location of the z probes in the dee. The direction of travel of the probes are indicated by the arrows. The dashed line shows a typical beam trajectory. Figure 14, an enlarged view of Fig. 13, gives the various distances between the probes and the ion source chimney.

1.7.2 Radial Emittance Area Probes

The radial emittance areas are found with the aid of two probes. The emittance area measuring process is described in Sec. 2.2. The first probe, located at the 90° beam position, is a 0.025" vertical slit. The slit is made from 1/8" tantalum and the tantalum is clamped to a horizontally moving probe. The 90° slit is remotely adjusted over a 4.00" range. A counter is geared to the slit adjusting knob and the position is known to $\pm$ 0.005".

The second probe is a differential current probe (0.015" diameter tantalum wire) and its position was determined experimentally. The top of Fig. 15 shows the trajectories of three ions with the same energy in a uniform magnetic field but having different angular divergence. The center of Fig. 15 shows the aberration occurring at the 180° focus point (dashed line), i.e., the top ray crosses the central ray before the focus point. Likewise, the bottom ray crosses the central ray after the focus point. The bottom of Fig. 15

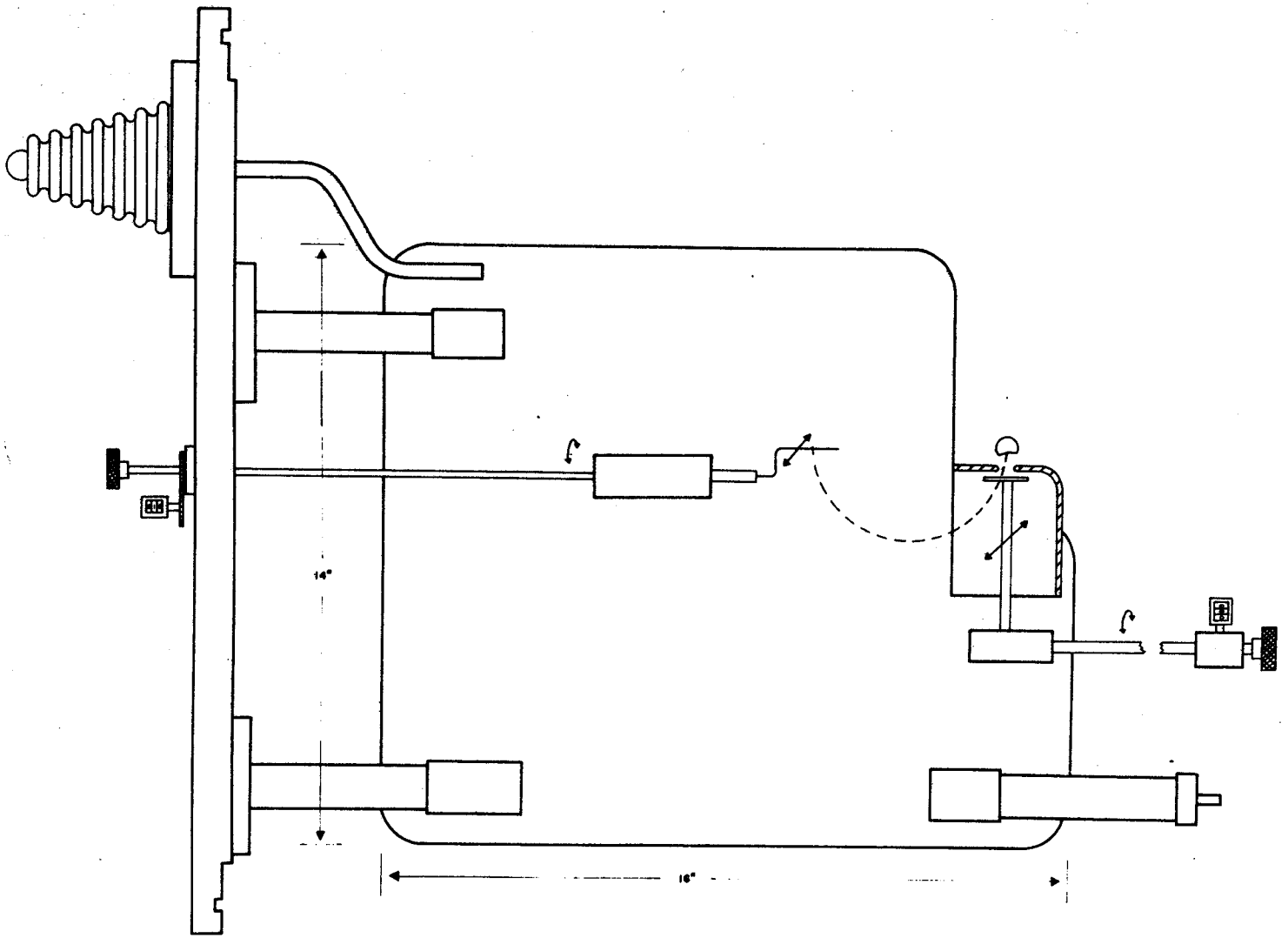

Fig. 13: Relative location of the axial probes in the dee. The directions of probe movement are indicated by the arrows (slant arrow indicates vertical motion). Counters are attached to the probes and allow probe position determination to ± 0.005". A typical beam trajectory is indicated by the dashed line.

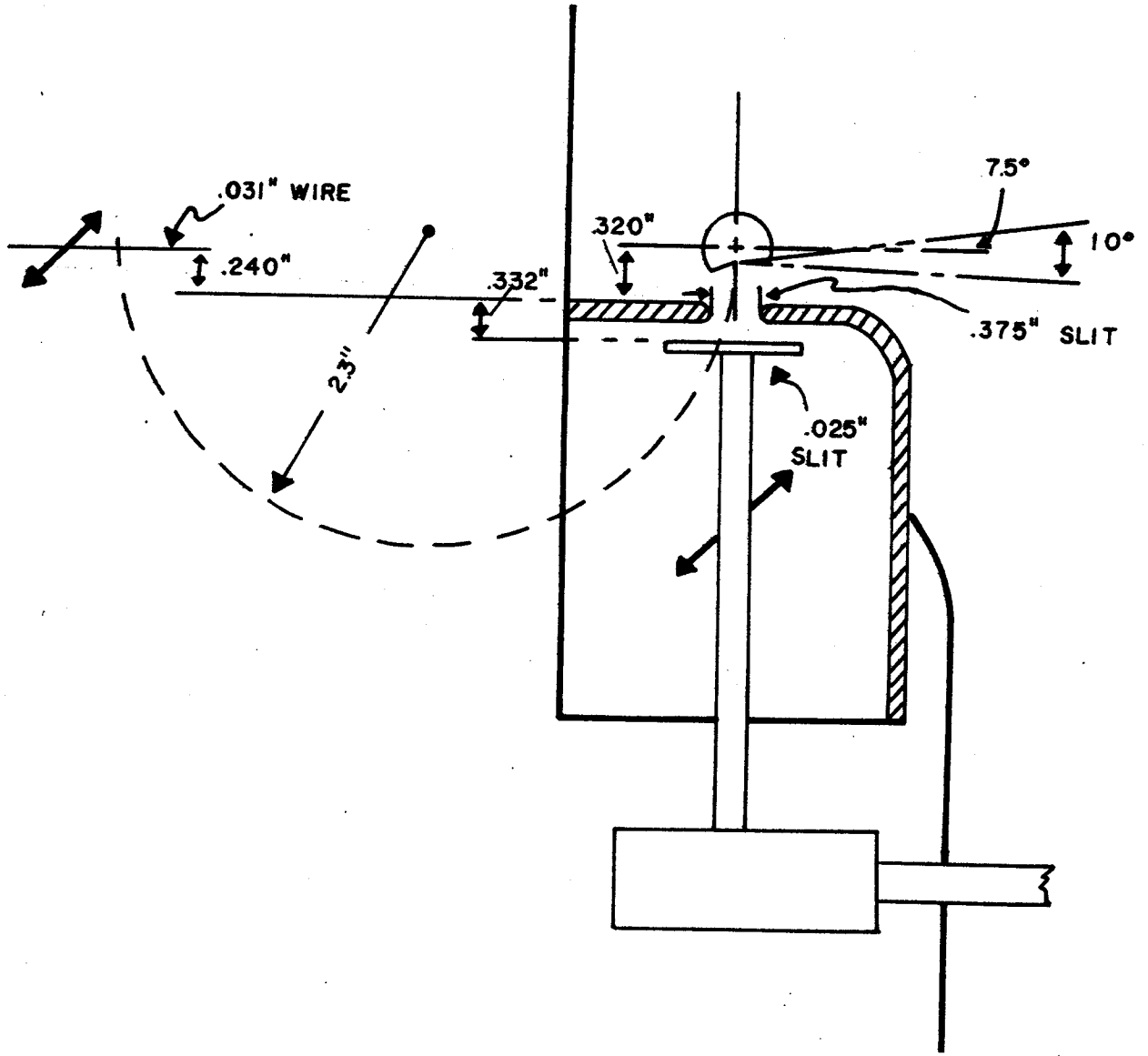

Fig. 14: Enlargement of Fig. 13. The various distances of the probes with respect to the ion source chimney are shown.

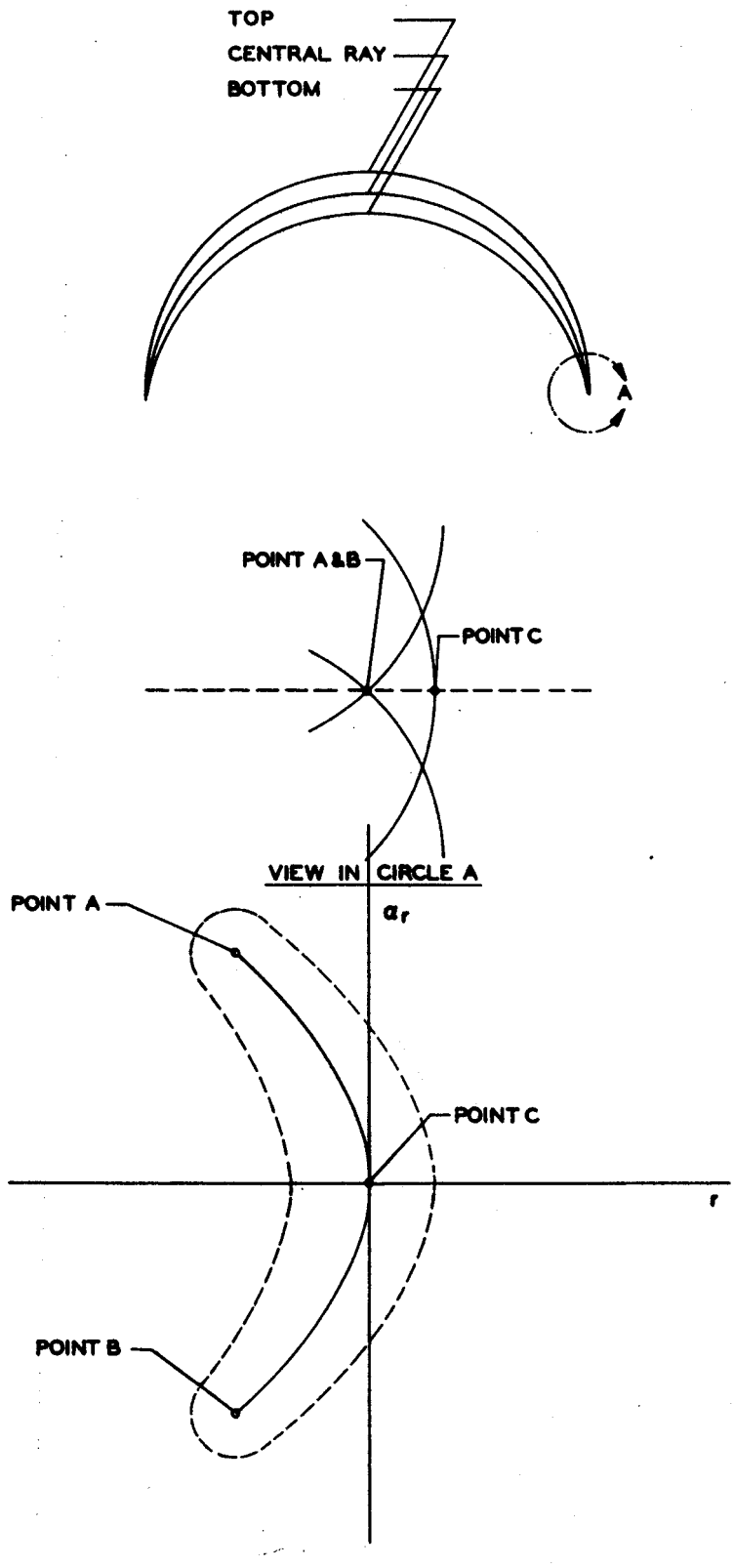

Fig. 15: Top: Three orbits starting with different angular divergence. Center: Enlarged view of 180° focus point (dashed line). The top ray crosses the central ray before the focus, while the bottom ray crosses the central ray after the focus. Bottom: The radial emittance area measured at the 180° focus. The top ray maps into point A. Likewise, the bottom ray goes into point B and the central ray into point C. The dashed-line area is the expected radial emittance area for a line source.

illustrates the radial emittance area measured for the three rays with a probe located at the 180° focus. Namely, the top ray maps into point A, the central ray into point C and the bottom ray into point B. The dashed-line area in the bottom of Fig. 15 shows the emittance area expected for a line source. Figure 16 shows the radial emittance area measured for three different locations (relative positions 0.000", 0.150" and 0.250") of the 180° differential probe. From the symmetry of the emittance areas in Fig. 16, the probe was located at a relative position of 0.150".

Figure 17 shows the position of the probes in the dee and their direction of motion as indicated by the arrows. Figure 18, an enlarged view of Fig. 17, gives the various distances between the probes and the ion source chimney. A typical ion trajectory is indicated by the dashed line.

1.7.3 Space Charge Probes

The 180° axial differential current probe (Sec. 1.7.1) was the only probe used in the space charge measurement. The position of the probe with respect to the chimney is shown in Fig. 14.

1.7.4 Radial Asymmetry Probes

Three probes were used to measure the radial asymmetry. The first probe, located behind the puller, is a 0.010" vertical slit (0° slit). The 0° slit is made from 1/8" tantalum, and the tantalum is clamped to a horizontally moving probe. The horizontal position of the 0° slit is remotely adjustable

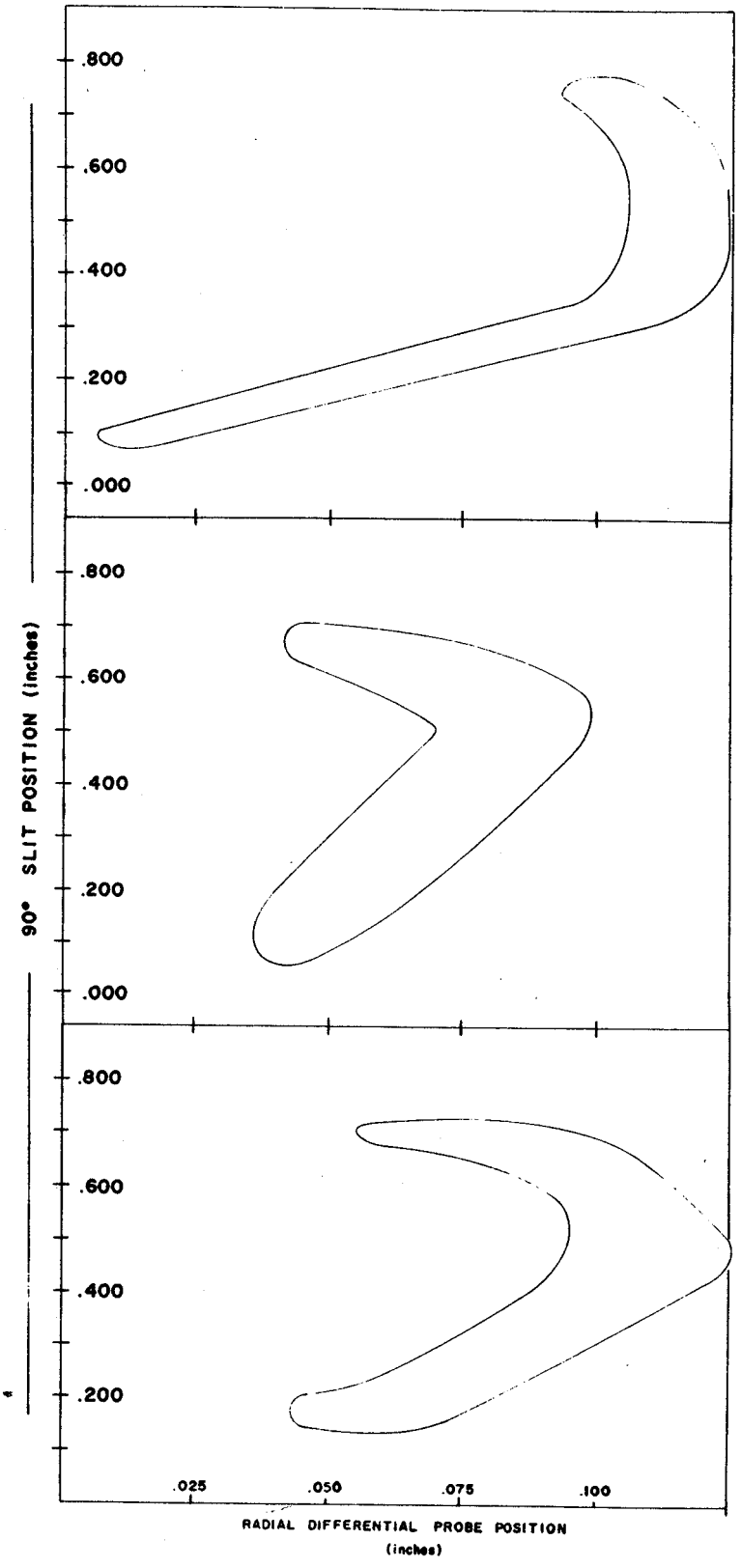

Fig. 16: Three radial emittance areas for different positions of 180° radial probe. The top is located at a relative position of 0.000", center at 0.120", and bottom at 0.250". The final position for the probe was chosen to be 0.150" and its position in the dee with respect to the chimney is indicated in Fig. 18.

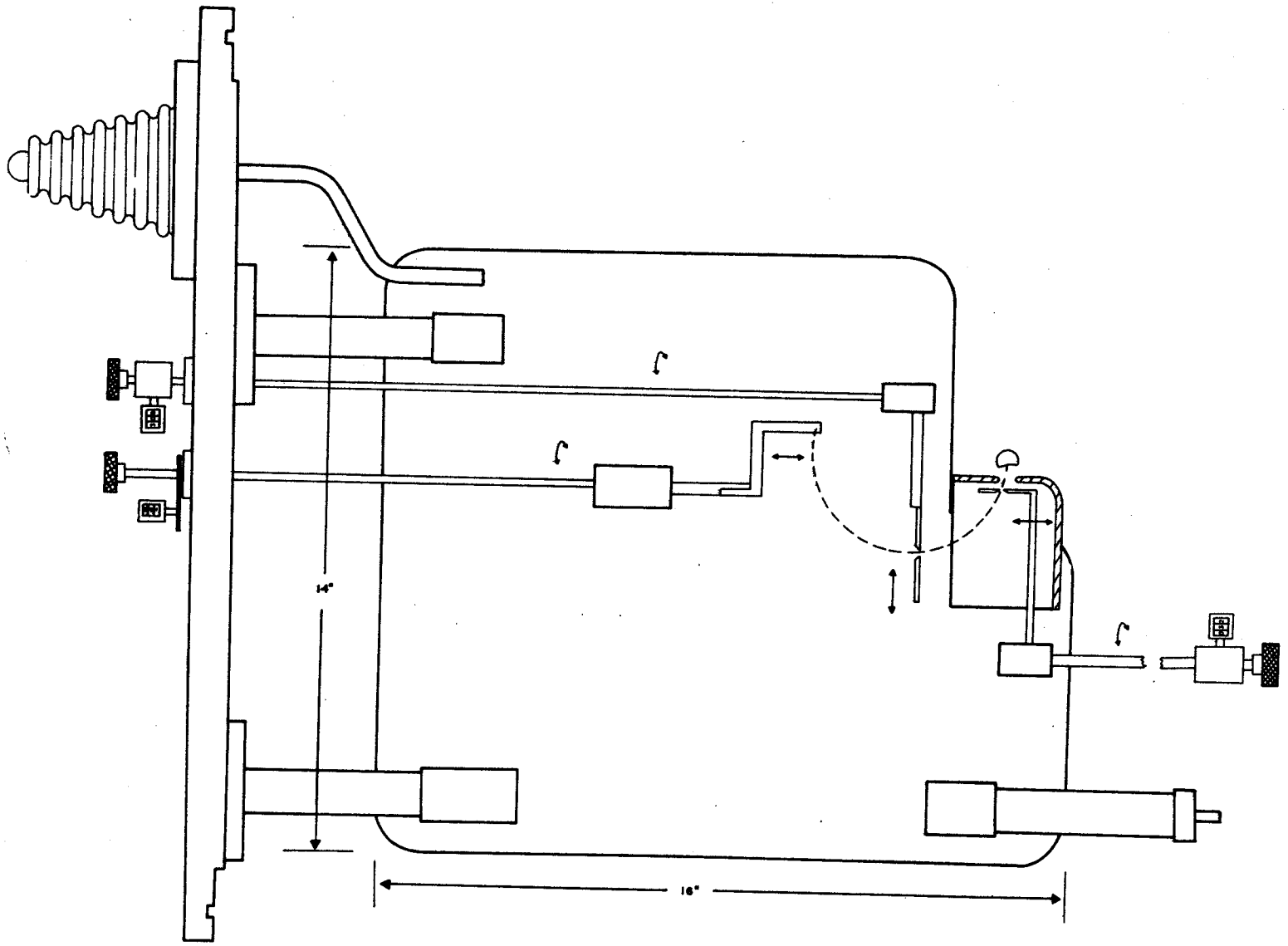

Fig. 17: Relative location of the radial probes in the dee. The probes direction of movement are indicated by the arrows. Counters are attached to each probe and allow probe position determination to ± 0.005".

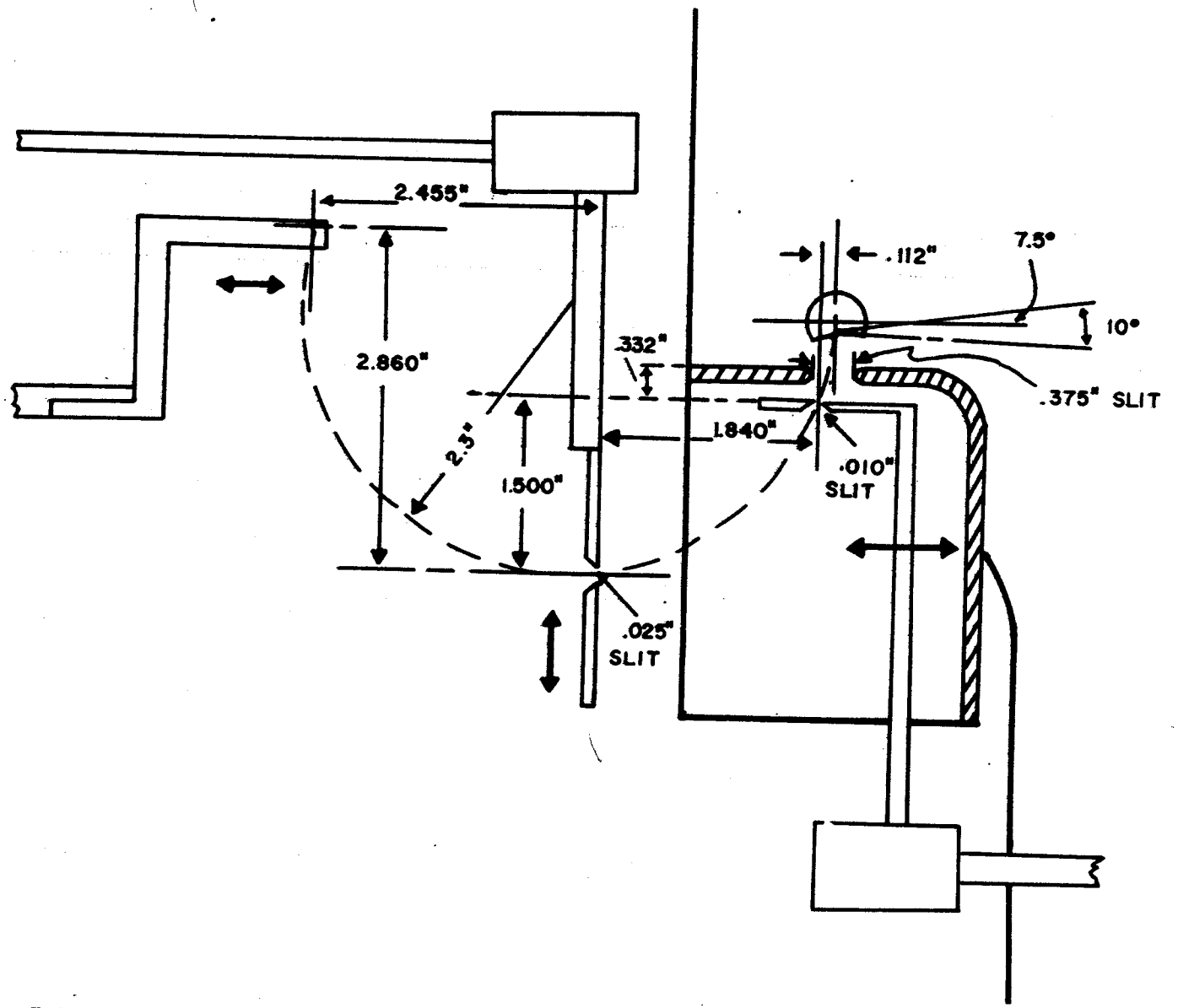

Fig. 18: Enlarged view of Fig. 17. The various distances of the probes with respect to the ion source chimney are shown.

over the full beam width. The slit adjusting knob is geared to a counter and allows the position to be determined to $\pm$ 0.005". The second probe is the 90° slit described in Sec. 1.7.2. The third probe, located at 180° beam position, is an integral current probe. It is a water-cooled tantalum sheet 1" x 2" x 1/8". The position of the probe is such that any protons passing through the 90° slit will be detected. Baffles are inserted in front of the current probe to stop all other ions. Figure 18 gives the various distances for the probes with respect to the ion source chimney.

1.7.5 Differential Current Probe Calibration

The beam current must be known accurately for the corresponding radial and axial emittance areas in the luminosity calculations. The differential current probe used in the emittance measurements gave an artificially high current reading due to secondary electron loss. To determine the detection efficiency for the differential current probe, a series of comparison measurements were made with an integral current probe. The integral probe had previously been checked for secondary electron loss by applying a potential to the probe in a Faraday-cup arrangement. Figure 19 shows the integral current versus the differential current for the same experimental conditions. The slope of the curve was found in a least square fit to be 0.704.

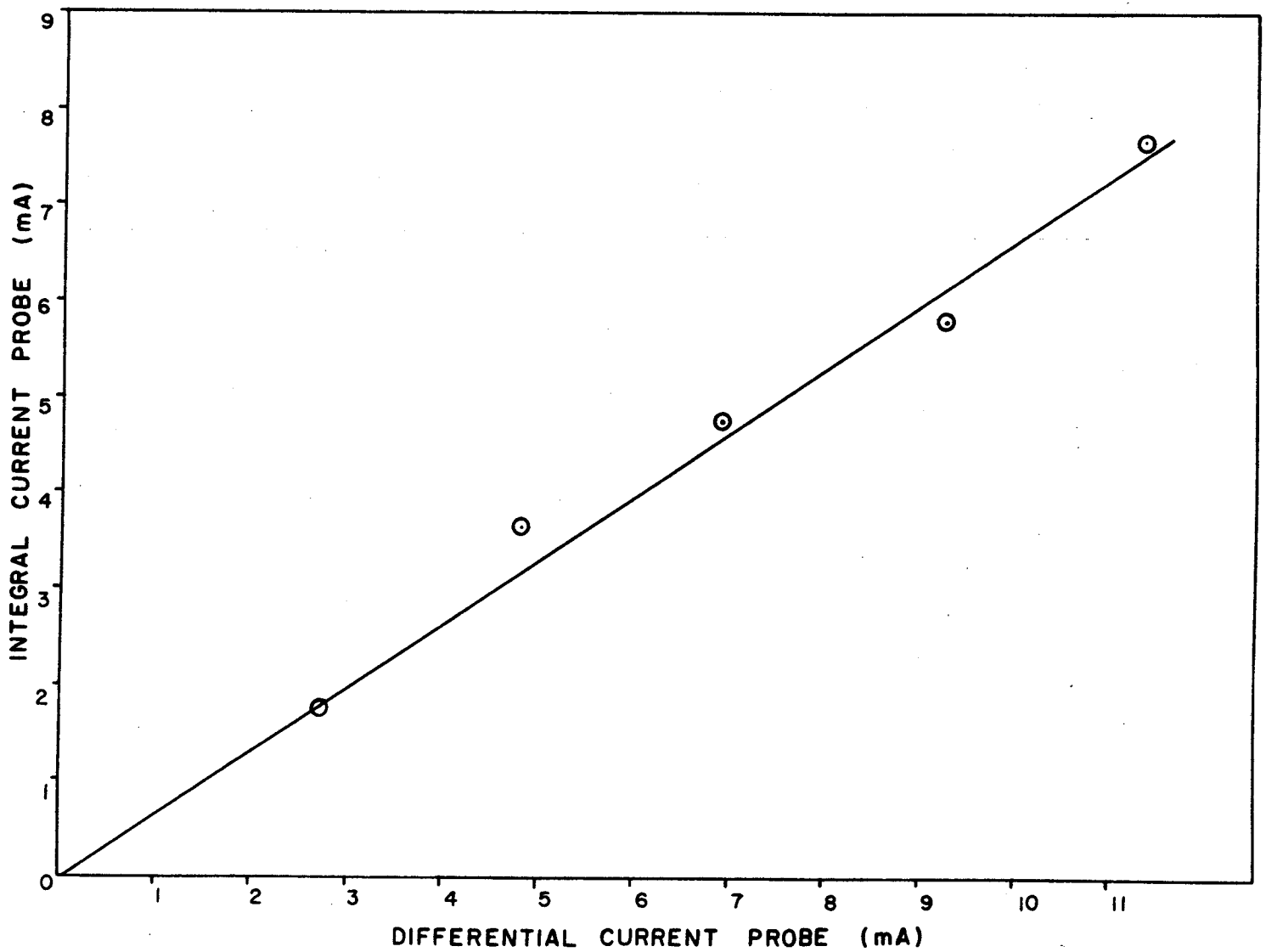

Fig. 19: Calibration curve of differential current probe versus integral current probe. The differential current probe gave an artificially high reading due to secondary electron loss. The slope, found in a least square fit, equals 0.704.

1.8 Ion Source and Dee Alignment

The horizontal alignment of the ion source and the dee was accomplished by two special fixtures. The first, an aluminum block (1" cube), has a projection that fits into the puller slit. Two crosshairs were scribed on top of the block at the location of the ion source center. The second special fixture is a copper tube of the same diameter as the ion source. A piece of plexiglass with crosshairs to denote the center of the ion source was placed in one end of the copper tube. The copper tube is inserted in place of the ion source, and the position of the puller adjusted (i.e., the puller cross slide adjusted) until the crosshairs of the aluminum block (mounted in the puller slit) lined up with the crosshairs of the copper tube. All slit positions inside the dee were measured with respect to the puller slit and, hence, known with respect to the ion source center. The copper tube included a pointer on its top indicating the direction of a crosshair. A marker on top of the ion source insertion tube was aligned with the pointer. A corresponding pointer on the ion source lines up with the marker (see Fig. 2).

The plasma boundary in the z direction provides a strong focusing momentum to the top and bottom of the ion beam as it emerges from the chimney (discussed in Sec. 2.4). A small change in the vertical position of the dee ($\pm$ 0.010") caused large changes in the focusing peaks. The final

vertical position of the dee was therefore adjusted to within $\pm$ 0.005" of the symmetric position of the focusing peaks.

II. EXPERIMENTAL RESULTS

2.1 Axial Emittance Measurements

The axial emittance area of the ion source is measured by letting the beam illuminate a narrow horizontal slit (see Sec. 1.7.1 for description of axial probes). The beam then axially spreads, with the amount of beam spread dependent upon the angular divergence of the beam and the distance from the 0° slit. Figure 20 below shows a two-dimensional projection of the axial motion of an ion in a magnetic field with an angular divergence, α_z, and where Δz is the beam spread measured by the 180° z probe.

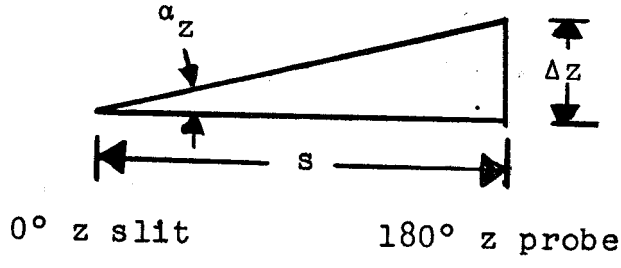

Fig. 20: Geometrical relations for deriving Eq. (7). Above, s is the orbit length between the 0° and 180° axial probes and Δz is the measured beam height at the 180° probe position.

The relation between the angular divergence and the beam spread, as shown in Fig. 20, is derived in Eq. (7).

$$\alpha_z = \sin^{-1} \frac{\Delta z}{s} \tag{7}$$

where s is the particles path length in traveling between the 0° z slit and the 180° probe. For this series of measurements s equals 7.401". Using Eq. (7) the angular divergence is determined by measuring the 180° axial beam spread.

However, the effect of axial focusing could result in an error in the measurement of α_z. Therefore, axial focusing was checked in a series of computer runs. The axial motion for a particle starting in the median plane and axially displaced (0.150") was calculated for initial angles of 0°, $\pm$ 1/2° and $\pm$ 1°. The maximum effect of the focusing force was observed for the + 1° particle starting at 0.150" and resulted in a 5% change in the measured angular divergence. This correction is small and was neglected in the axial emittance area measurements.

Figure 21 shows typical data for a complete scan of 0° z slit positions (steps of 0.025"). Each curve represents the beam spread at the 180° position for a given position of the 0° z slit, e.g., curve #1 is the top of the beam and curve #12 the bottom. The 100% angular divergence for each peak is obtained from its width at zero current and Eq. (7). Table II lists the angular divergences for Fig. 21.

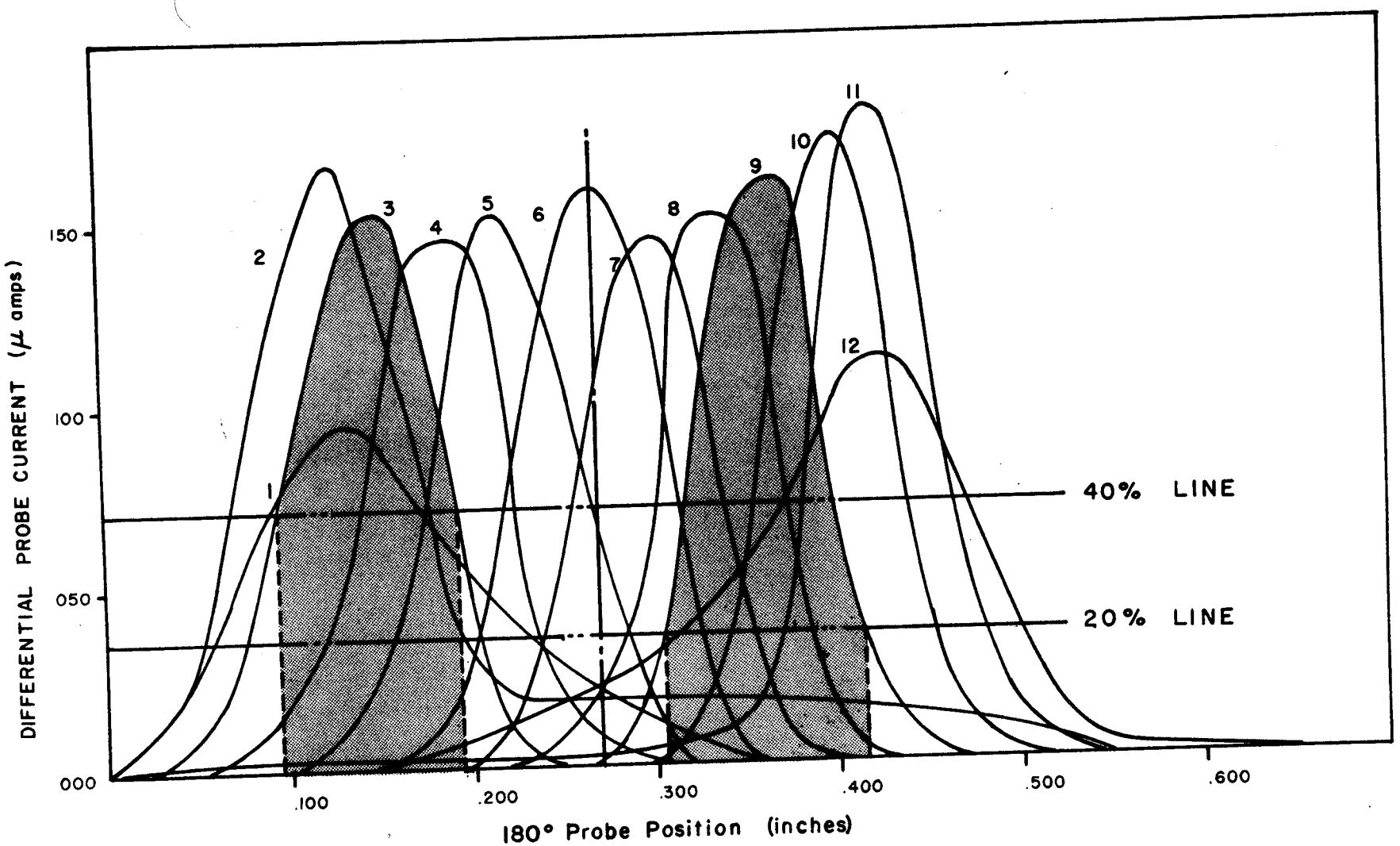

Fig. 21: Axial emittance area data for a complete scan of the 0° z slit for a 0°-L chimney at 1 amp arc current. Each curve is the 180° measured beam spread for a different position of the 0° z slit. The vertical line in curve #6 is the position of the 0° z slit for a measurement of curve #6. Density contours are found for lines drawn at 20% and 40% of the maximum current in curve #6. Current areas for the 20% and 40% lines are indicated in curves #9 and #3.

Table II: The axial angular divergence data determined from Fig. 21. The last two columns can be converted into milliradians by using Eq. (7).

Fig. 21 Curve Number	180° Probe Positions			Positive Angular Divergence (inches)	Negative Angular Divergence (inches)
	Zero Angular Divergence (inches)	Right Zero Current (inches)	Left Zero Current (inches)		
1	0.415	0.610	0.130	0.195	0.285
2	0.390	0.525	0.315	0.135	0.075
3	0.365	0.520	0.300	0.155	0.065
4	0.340	0.460	0.260	0.120	0.080
5	0.315	0.415	0.220	0.100	0.085
6	0.290	0.380	0.200	0.090	0.090
7	0.265	0.350	0.155	0.085	0.110
8	0.240	0.315	0.100	0.075	0.140
9	0.215	0.300	0.055	0.085	0.160
10	0.190	0.250	0.015	0.060	0.175
11	0.165	0.525	0.025	0.360	0.140
12	0.140	0.375	-0.050	0.235	0.190

The vertical line (Fig. 21, curve #6) indicates the position of the 0° z slit for curve #6, and is the position of zero angular divergence. The position of zero angular divergence for all other peaks corresponds to some multiple shift of 0.025" of the 0° z slit with respect to its position at curve #6. The emittance area obtained from Fig. 21 appears in Fig. 22 and equals 278 mm-mrad for a current of 4.24 mA.

Current density contours of the emittance areas were made for all measurements. A new angular divergence is found for each peak at an arbitrary fraction of the peaks intensity. For instance, Fig. 21 shows lines drawn for 20% and 40% of the maximum current of curve #6. Tables III and IV list the angular divergences determined from the peak widths at the 20% and 40% lines of Fig. 21. The corresponding emittance areas, plotted in Fig. 22, are 126.3 and 98.7 mm-mrad, respectively.

The current for the density contours is equal to the current contained within the new angular divergence. The current within one peak for the 20% line angular divergence is illustrated by the shaded area in Fig. 21 (curve #9). A corresponding area exists for each curve, and each current area was measured by a polar planimeter and the total current found from the sum of all curves. Also illustrated in Fig. 21 is the current of one curve for a 40% line (curve #3). The currents found for the 20% and 40% lines are 3.71 and 3.27 mA corresponding to 87.5% and 77% of the current, respectively.

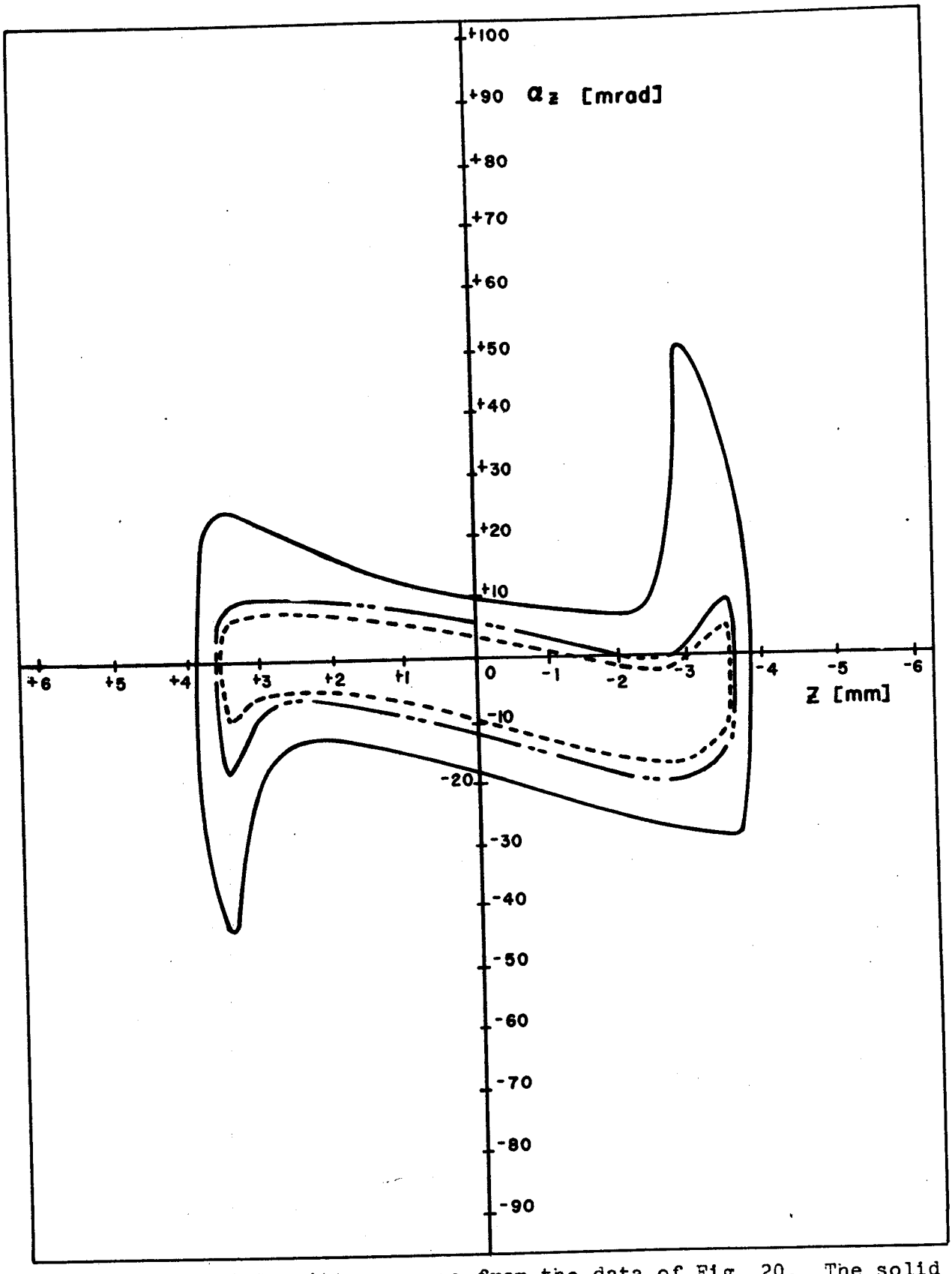

Fig. 22: The axial emittance area from the data of Fig. 20. The solid line is the 100% current (4.24 mA) emittance area and equals 278 mm-mrads. The inner lines are density contours for 87.5% and 77% of the current and equals 126.3 and 98.7 mm-mrad, respectively.

Table III: The axial angular divergence data determined from the intersection of the curves with the 20% line in Fig. 21.

Fig. 21 Curve Number	180° Probe Positions			Positive Angular Divergence (inches)	Negative Angular Divergence (inches)
	Zero Angular Divergence (inches)	Right Zero Current (inches)	Left Zero Current (inches)		
1	0.415	0.498	0.310	0.083	0.105
2	0.390	0.475	0.365	0.085	0.035
3	0.365	0.450	0.340	0.085	0.025
4	0.340	0.412	0.302	0.072	0.038
5	0.315	0.388	0.280	0.073	0.035
6	0.290	0.355	0.240	0.065	0.050
7	0.265	0.325	0.200	0.065	0.065
8	0.240	0.285	0.155	0.045	0.085
9	0.215	0.240	0.115	0.025	0.100
10	0.190	0.202	0.075	0.012	0.115
11	0.165	0.195	0.050	0.030	0.115
12	0.140	0.225	0.057	0.085	0.083

Table IV: The axial angular divergence data determined from the intersection of the curves with the 40% line in Fig. 21.

Fig. 21 Curve Number	180° Probe Positions			Positive Angular Divergence (inches)	Negative Angular Divergence (inches)
	Zero Angular Divergence (inches)	Right Zero Current (inches)	Left Zero Current (inches)		
1	0.415	0.477	0.370	0.062	0.045
2	0.390	0.460	0.372	0.070	0.018
3	0.365	0.440	0.350	0.075	0.015
4	0.340	0.400	0.315	0.060	0.025
5	0.315	0.375	0.290	0.060	0.025
6	0.290	0.345	0.250	0.055	0.040
7	0.265	0.320	0.210	0.055	0.055
8	0.240	0.275	0.170	0.035	0.070
9	0.215	0.230	0.135	0.015	0.080
10	0.190	0.195	0.090	0.005	0.100
11	0.165	0.180	0.065	0.015	0.100
12	0.140	0.190	0.080	0.050	0.060

Various measurements were repeated for the axial emittance areas and produced agreement to within ± 2%. The current, however, varied for repeated measurements by ± 6%. To try and understand the current variation, a systematic change was made on the ion source gas flow and arc voltage. Results showed that for a change of ± 0.5 cc/min from 1.5 cc/min the current changed by ± 3.5% at 1 amp arc current. Also the current changed by ± 5.7% for an arc voltage change of ± 5 volts from 100 volts. The small variation of the gas flow and arc voltage, which are difficult to control experimentally, account for the measured current differences.

Tables V and VI include results of the axial emittance areas for the different chimney configurations (see Fig. 23 for chimney geometry changes) at 1 and 5 amps. The data suggest that the emittance area for 100% current becomes smaller as the angle changes from 0° to 20°. The effect of chimney barrel size appears to be small in the axial measurements. Table VII is the emittance areas for a 10° small barrel chimney as a function of arc current (1 to 5 amps) and indicates that the emittance area for 100% current increases with the arc current.

Figure 24 illustrates the emittance areas for a 0°, 10° and 20° chimney. The chimney face angle effect on emittance areas appears as a rotation of the areas about zero angular divergence, namely, the 0° emittance area is rotated clockwise about zero momentum. This leads to a beam defocusing, i.e., for the top of the beam (+ z) the total angular divergence

Table V: The axial emittance areas for 100%, 85% and 70% currents for different chimney configurations at 1 amp arc current.

Chimney Type*	Emittance Area for 100% Current		Emittance Area for ~85% Current		Emittance Area for ~70% Current	
	Area mm-mrad	Current mA	Area mm-mrad	% Current	Area mm-mrad	% Current
0°-L	278	4.24	126	88	90	77
0°-S	279	3.22	114	89	85	73
10°-L	271	1.67	92	80	57	65
10°-S	256	1.93	95	82	57	68
20°-L	225	1.25	87	80	49	62

* The degrees indicate the angle of recessing of the chimney slit from a flat face source. S means chimney barrel diameter of 0.500"; L means chimney barrel diameter of 0.720".

Table VI: The axial emittance areas for 100%, 85% and 70% currents for different chimney configurations at 5 amps arc current.

Chimney Type*	Emittance Area for 100% Current		Emittance Area for ~85% Current		Emittance Area for ~70% Current	
	Area mm-mrad	Current mA	Area mm-mrad	% Current	Area mm-mrad	% Current
0°-L	379	9.88	151	85	97	69
0°-S	390	12.74	166	86	111	72
10°-L	286	6.06	127	84	81	68
10°-S	278	7.99	122	85	76	70
20°-L	299	5.55	120	83	80	68

* The degrees indicate the angle of recessing of the chimney slit from a flat face source. S means chimney barrel diameter of 0.500"; L means chimney barrel diameter of 0.720".

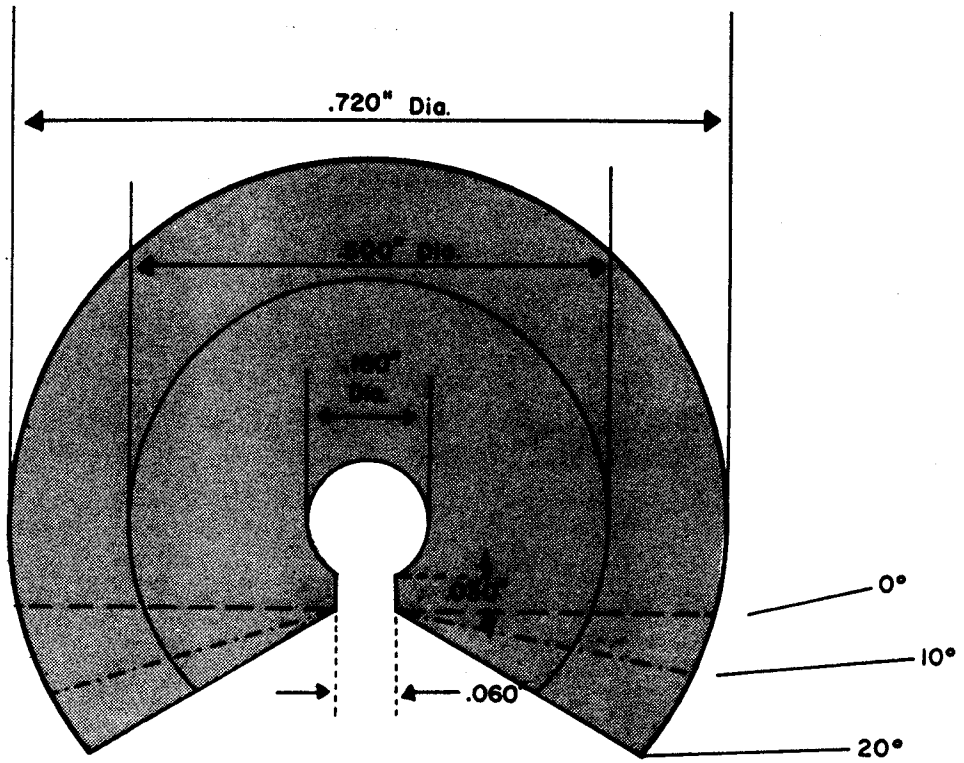

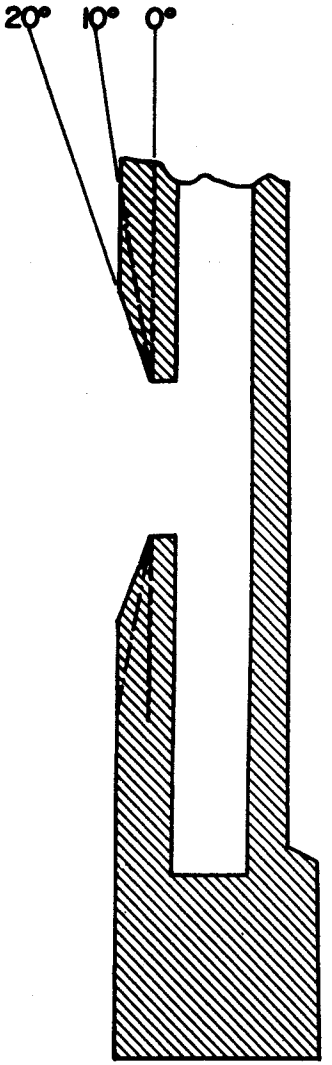

Fig. 23: Median plane and axial cross section of ion source chimney. The chimney geometrical changes are the following: barrel diameter, 0.720" to 0.500" and face angle, 0° to recessed slits of 10° and 20°

Table VII: The axial emittance areas for 100%, 85% and 70% currents for a 10°-S chimney at various arc currents.

Arc Current	Emittance Area for 100% Current		Emittance Area for ~85% Current		Emittance Area for ~70% Current	
	Area mm-mrad	Current mA	Area mm-mrad	% Current	Area mm-mrad	% Current
1	221	1.93	95	82.4	57	67.5
2	212	3.39	103	85.4	69	72.6
3	227	4.87	118	86.4	78	72.6
4	262	6.52	123	85.5	73	69.0
5	277	7.99	123	85.3	76	69.6

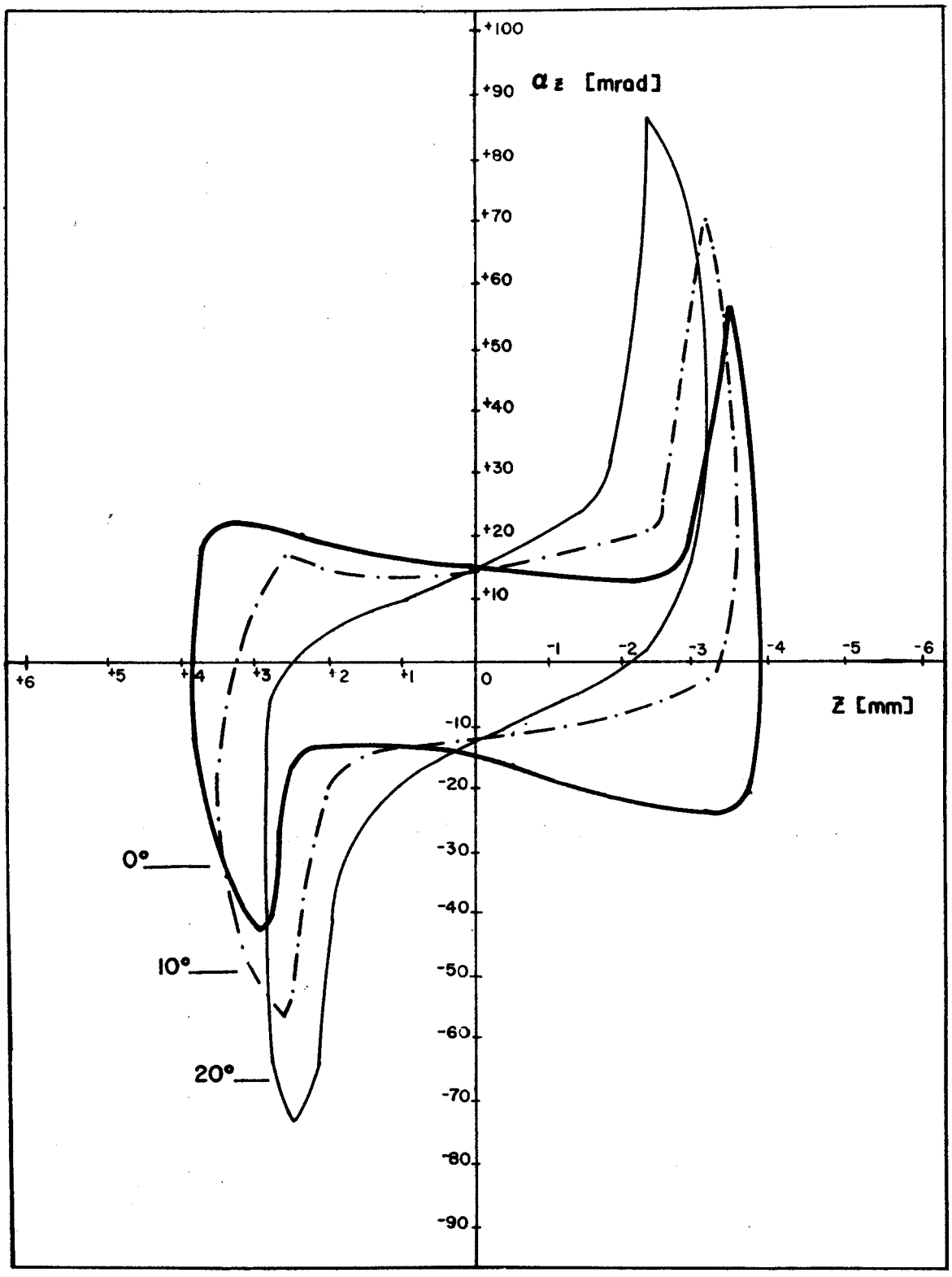

Fig. 24: The effect of chimney face angle on axial emittance area. Changing the chimney face angle causes the emittance area to rotate about zero angular divergence. Namely, the 0° emittance area is rotated clockwise about zero, leading to a beam defocusing condition. Conversely, the 20° emittance area is rotated counterclockwise, producing a beam focusing condition.

is positive and likewise for the bottom of the beam (- z) the total angular divergence is minus, hence defocusing. Conversely, the 20° emittance area is rotated counterclockwise about zero angular divergence producing a beam focusing condition, i.e., for the top of the beam (+ z) the total angular divergence is negative and likewise opposite for the bottom of the beam, hence focusing. The rotations of the axial emittance areas are in good agreement with a series of computer studies made by M. Reiser[8]. He studied the effect of the chimney face angle on radial beam focusing where the radial approximations are valid in the axial direction for this experiment.

2.2 Radial Emittance Area Measurements and Results

The measurements of the radial emittance areas are similar to the axial measurements. However, in the radial case the uniform magnetic field causes the particles to be focused at $N\lambda/2$, where N is an integer and λ is the radial betatron oscillation wavelength. For a uniform field (no aberrations) λ is one revolution or 360°. The maximum beam spread resulting from different initial angular divergences occurs at $(2N + 1)\lambda/4$ oscillation and hence the radial emittance area angular divergence probe was located at 90°. The relation for a given initial angular divergence, α_r, and a beam spread h at 90° is shown in Fig. 25 and given in Eq. (8).

Fig. 25: Geometrical relation for deriving Eq. (8). The angular divergence, α_r, at 0° results in a beam spread, h, at 90°. The radius of curvature, ρ, is calculated for a - 30 kV dee potential and 4.2 kG magnetic field.

$$\alpha_r = \sin^{-1} \frac{h}{\rho} \qquad (8)$$

where α_r is small. The radius of curvature, ρ, is calculated from the known magnetic field and dee voltage.

The radial width probe was located at 180° (λ/2) and the procedure used to locate the probe position was as described in Sec. 1.7.2. Again a set of curves were obtained for the complete scan of the 90° slit (quite similar to Fig.

21) and the radial emittance areas were determined from the curves using the same procedure as in the axial case.

Figure 26 illustrates a typical measured radial emittance area having an area of 370 mm-mrads. The dashed lines indicate density contours obtained for 90% and 70% of the total beam current. The density contour areas equal 206 and 131 mm-mrad, respectively. Tables VIII and IX are the radial emittance area results for different chimney configurations (see Fig. 23 for chimney changes) at 1 and 5 amps arc currents. The radial emittance areas decrease as the chimney face angle changes from 0° to 20° for a given arc current. Also, the radial emittance area is smaller for the 0.500" chimney barrel as compared to the 0.720" barrel. Table X is the radial emittance area for the 10°-S (0.500" barrel) chimney for arc currents of 1 to 5 amps and indicates that radial emittance area increases with arc current. Several radial emittance areas were measured again and reproduced to within $\pm$ 5%.

2.3 Luminosity

The emittance data in combination with the current measurements, allows evaluation of the luminosity. Figure 27 gives the luminosity for the 10°-S chimney at different arc current values. The data indicated that the luminosity increases approximately linearly with arc current. Table XI

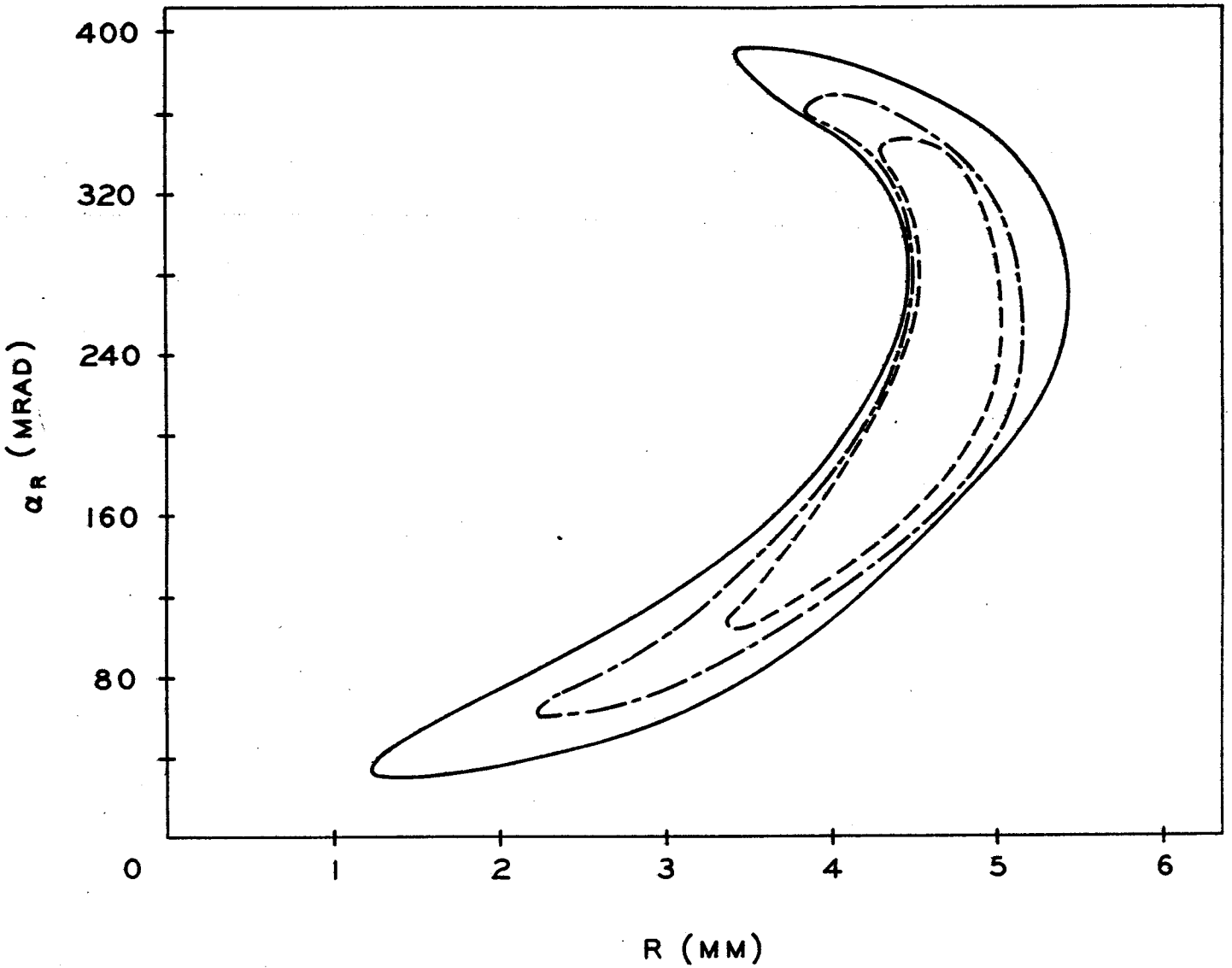

Fig. 26: The radial emittance area for a 0°-L chimney at 1 amp arc current. The solid line is the 100% current emittance area (370 mm-mrad). The inner dashed lines are density contours for 90% and 70% of the current and the areas are 206 and 131 mm-mrad, respectively.

Table VIII: The radial emittance areas for 100%, 90% and 85% currents for different chimney configurations at 1 amp arc current.

Chimney Type*	Emittance Area for 100% Current		Emittance Area for ~90% Current		Emittance Area for ~85% Current	
	Area mm-mrad	Current mA	Area mm-mrad	% Current	Area mm-mrad	% Current
0°-L	370	4.24	207	90	131	70
0°-S	312	3.22	216	95	166	86
10°-L	293	1.67	196	96	145	85
10°-S	293	1.93	195	95	152	87
20°-L	194	1.25	146	97	118	87

* The degrees indicate the angle of recessing of the chimney slit from a flat face source. S means chimney barrel diameter of 0.500"; L means chimney barrel diameter of 0.720".

Table IX: The radial emittance areas for 100%, 90% and 70% currents for different chimney configurations at 5 amps arc current.

Chimney Type*	Emittance Area for 100% Current		Emittance Area for ~90% Current		Emittance Area for ~70% Current	
	Area mm-mrad	Current mA	Area mm-mrad	% Current	Area mm-mrad	% Current
0°-L	525	9.88	309	84	172	66
0°-S	404	12.74	224	93	132	68
10°-L	478	6.06	262	92	156	74
10°-S	436	7.99	215	90	141	71
20°-L	307	5.55	183	91	114	73

* The degrees indicate the angle of recessing of the chimney slit from a flat face source. S means chimney barrel diameter of 0.500"; L means chimney barrel diameter of 0.720".

Table X: The radial emittance areas for 100%, 90% and 75% currents for 10°-S chimney at various arc currents.

Arc Current	Emittance Area for 100% Current		Emittance Area for ~90% Current		Emittance Area for ~75% Current	
	Area mm-mrad	Current mA	Area mm-mrad	% Current	Area mm-mrad	% Current
1	263	1.93	173	94.9	112	86.8
2	321	3.39	223	93.1	140	78.2
3	377	4.87	217	89.9	140	74.1
4	431	6.52	241	94.9	147	74.5
5	436	7.99	215	90.3	141	71.3

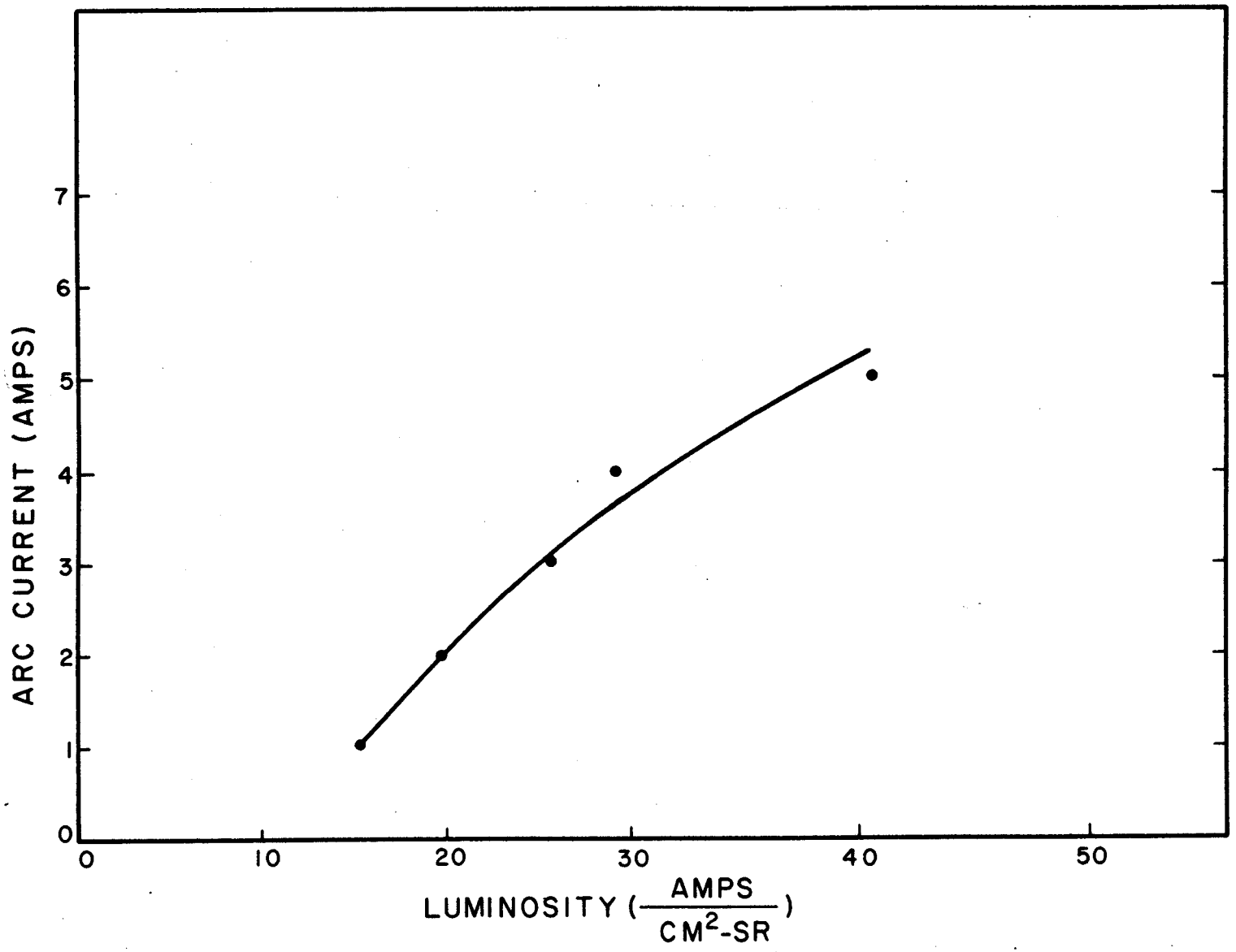

Fig. 27: Luminosity for a 10°-S chimney as a function of arc current. The luminosity is approximately linear versus arc current.

Table XI: The luminosity for ~ 85% current for different chimney configurations at 1 and 5 amps arc currents. Energy equals 30 kV.

Chimney Type*	Luminosity at 1 amp arc current ~ 85% current	Luminosity at 5 amps arc current ~ 85% current
	amps/cm^2-sr	amps/cm^2-sr
0°-L	22.2	33.5
0°-S	18.3	48.3
10°-L	11.6	23.9
10°-S	15.2	40.7
20°-L	12.2	33.2

* The degrees indicate the angle of recessing of the chimney slit from a flat face source. S means chimney barrel diameter of 0.500"; L means chimney barrel diameter of 0.720".

30 kilovolts per page 5

gives the luminosity for different chimneys at 1 and 5 amps arc current for ~ 85% beam current. As a function of chimney face angle, the luminosity is largest at 0°, approaches a minimum at 10° and then starts to increase again at 20°.

The luminosity estimated error is determined from the reproducibility of the current and emittance measurements and is found to be ± 15%. Nevertheless, comparison of a typical value from Table X with the previously estimated value of Blosser and Gordon[5] shows the measured value to be better by a factor of ten.

The result of the luminosity calculation may have a greater dependency upon parameters other than barrel size and chimney face angle. For instance, Livingston and Jones[9] have found that the position of the plasma column and the thickness of the chimney at the slit causes large variations in output current. This may account for the differences in measured luminosities. These factors should be investigated further.

2.4 Axial Plasma Boundary

The focusing peaks observed at the top and bottom of the axial emittance area as shown in Fig. 22 give rise to an interesting phenomenon, that can be attributed to a concave plasma boundary at the ends of the source slit. The left side of Fig. 28, a cross section of the chimney, shows

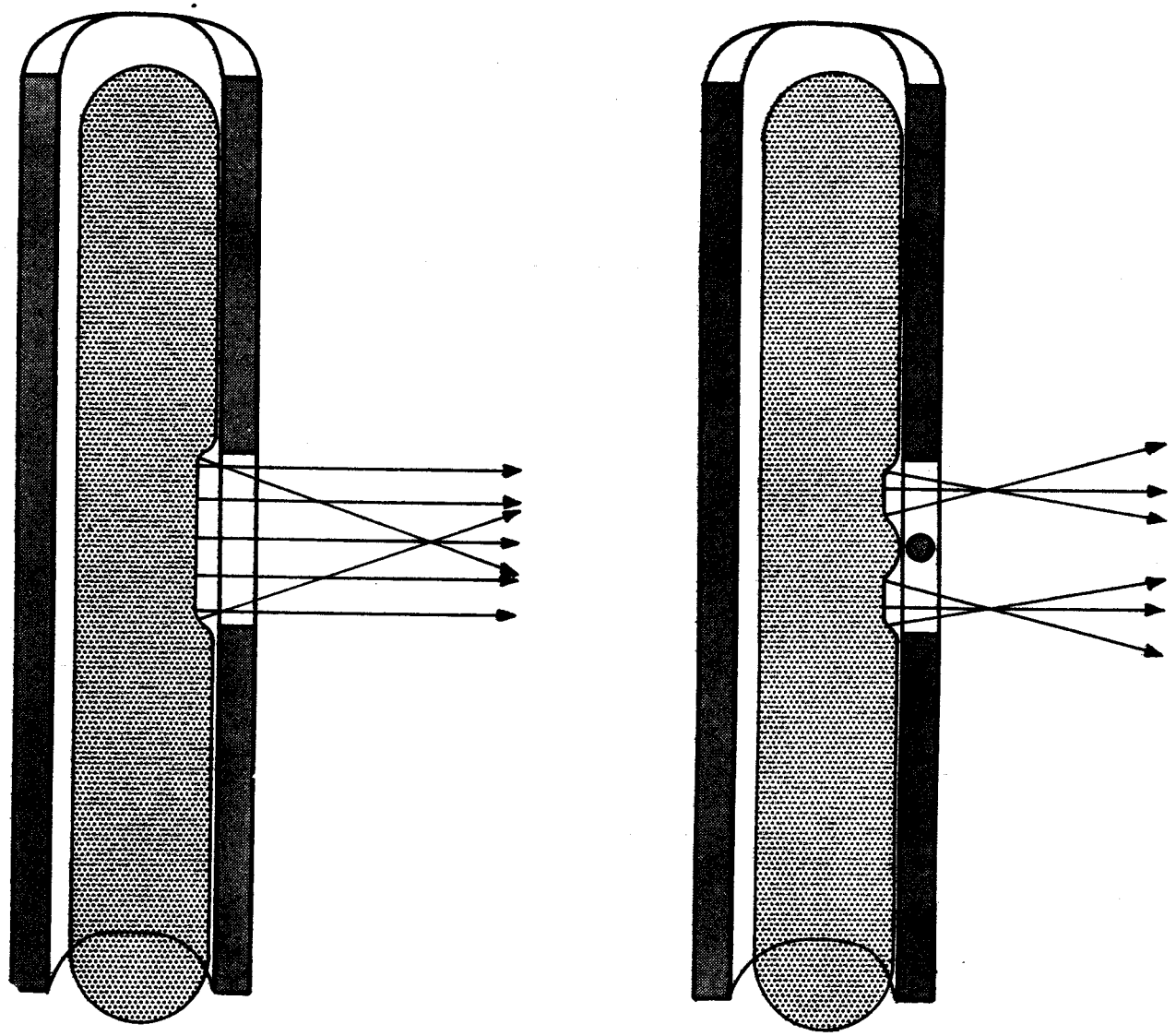

Fig. 28: Left side: Cross section of the chimney showing plasma curvature at chimney slit. The arrows represent ion trajectories and indicate that ions emitted at the top and bottom of the chimney slit from the concave plasma surface are focused toward the median plane. Right side: Cross section of chimney showing expected plasma surface with a 0.031" tantalum wire inserted in the center of the chimney slit. The plasma is now divided into two concave surfaces.

such a plasma curvature at the chimney slit. The arrows represent ion trajectories and indicate that ions emitted at the top and bottom of the chimney slit focus toward the median plane.

The right side of Fig. 28 illustrates a similar plasma boundary for a special chimney with a 0.031" diameter tantalum wire inserted in the center of the chimney slit. If the plasma surfaces are concave, insertion of the wire should cause the plasma boundary to form two concave surfaces. The axial emittance area would now divide into two sections, each section having two focusing peaks. Figure 29 gives the measured axial emittance area with the wire inserted in the chimney and shows two emittance areas, each with focusing peaks in accord with concave plasma surfaces.

2.5 Space Charge Effects

Space charge effects are apparent in an axial expansion of the beam at the 180° position and are a function of total current. Figure 30 gives the height of the beam at 180° probe versus total current, indicating that the axial height is approximately linear with total current for a given chimney angle. This agrees with the results of a derivation of MacKenzie[10]

$$I(\text{e.s.u.}) = \frac{h}{2} \frac{\phi}{(2\pi\omega)^3} \left(\frac{e}{m}\right)^2 \frac{V^3}{r_m^4}, \qquad (9)$$

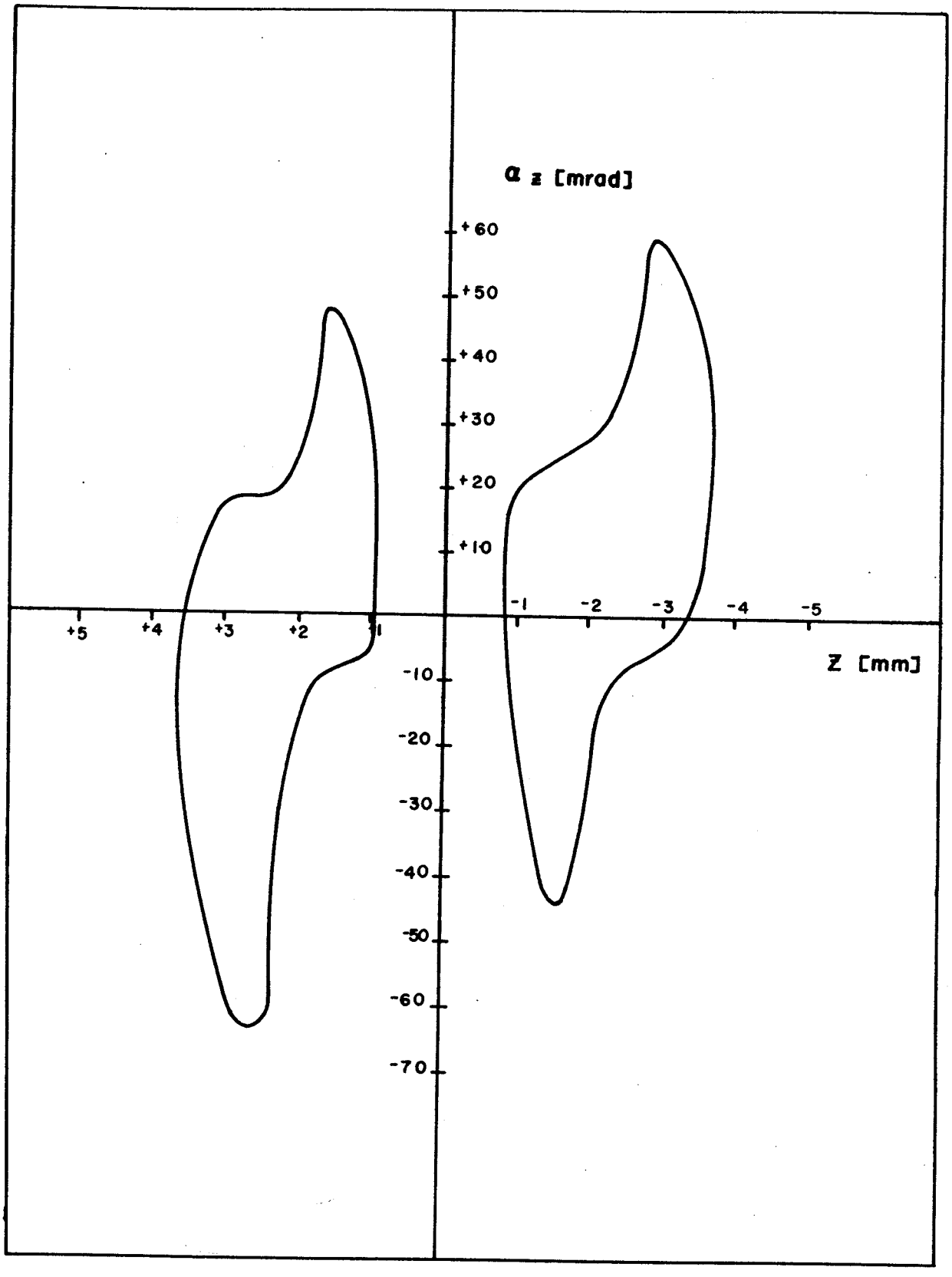

Fig. 29: The axial emittance area for the right side of Fig. 28. Two emittance areas were found, each with focusing peaks, and hence in accord with concave plasma surfaces.

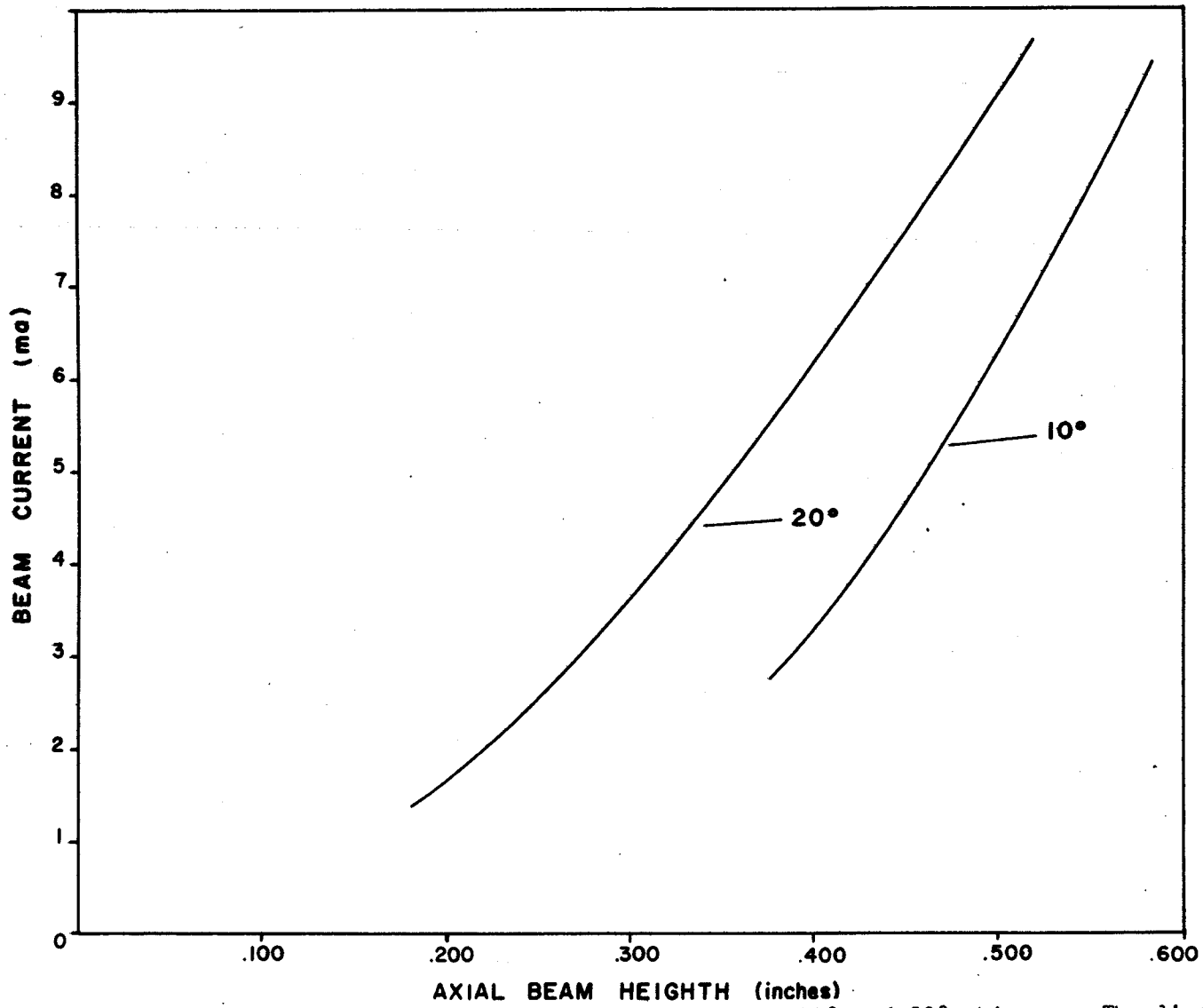

Fig. 30: Beam height at 180° versus total beam current for a 10° and 20° chimney. The linear results of the curves are in accord with space charge expectations. The focusing effect of the chimney face angle accounts for the shift between the 10° and 20° chimney measurements.

where I is the current arriving at a height h, V is the voltage per turn, ω the angular frequency, ϕ a fixed phase spread, and r_m is the radius at which magnetic focusing occurs*. The effects of electric field focusing are evidenced by the shift of the curves in Fig. 30 that occurs between the 10° and 20° chimneys. The obvious important result shown in Fig. 30 is that the chimney face angle can be used to give an electric focusing force.

2.6 Radial Emittance Asymmetry

An asymmetry was detected in the radial emittance area measurements as a function of arc current and was traced to a strain displacement of the ion source filament. Figure 31 shows the radial beam spread measured at 90° for 1 and 5 amps arc currents for different radial portions of the beam directly behind the puller. At 1 amp arc current (curve (a) of Fig. 31), the peak containing the maximum current is at the central radial position of the beam. The filament current was then increased until 5 amps arc current was obtained.

---

* MacKenzie's derivation assumes an elliptical charge distribution (Volume = $(\pi/2)zr\phi\delta r$) of total charge $Q = 2\pi I/\omega$. The force on an ion at a height z above the median plane is calculated for the above charge distribution. The magnetic focusing force on the ion is assumed to be zero up to radius r_m (an excellent approximation for the ion source testing facility). The ion axial displacement as a function of time is found by integrating the force equation.

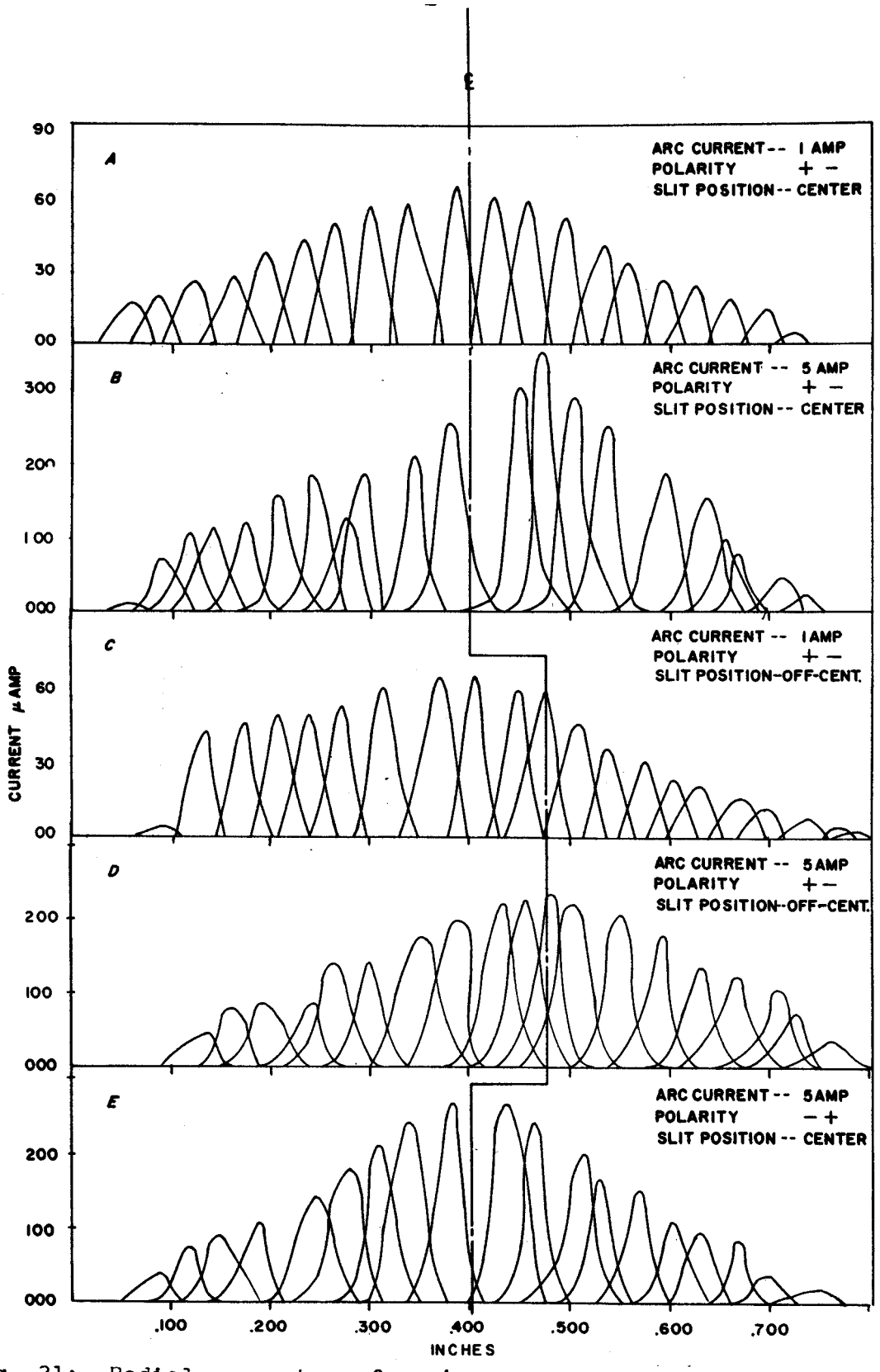

Fig. 31: Radial asymmetry of maximum current peak as a function of arc current (curves (a) and (b)). The center line, ℄L, of the beam passing through the 0° radial slit is indicated by the solid vertical line. Shifting the chimney slit (curves (c) and (d)) caused the maximum peak to move, indicating the plasma boundary is changing as the filament current is increased to a new arc current. Switching the direction of the filament current (curve (e)) caused the maximum current peak to shift in the opposite direction (cf. curve (b)).

The peak with maximum current (5 amps arc current) has shifted from the central position to the right (curve (b) of Fig. 31).

A new chimney with the slit shifted 0.010" to the left (see Fig. 9) was constructed and measurements made at 1 and 5 amps arc currents (curves (c) and (d) of Fig. 31). The results show the maximum current peak shifted to the left for 1 amp arc current. At 5 amps arc current the maximum peak is centered. These measurements indicate that the plasma shifts radially as the filament current increases.

Previously it had been observed that old filaments were slightly bent. The bending was a result of the force due to the interaction of the filament current and the magnetic field. The filament alignment with respect to the chimney slit and the direction of filament current can be seen in Fig. 9. The direction of the strain force ($\vec{F}$ in Fig. 9) is in the right direction to account for the radial plasma displacement detected in Fig. 31. Curve (e) of Fig. 31 shows a measurement taken with filament current reversed (cf. curve (b)) at 5 amps showing the maximum current peak shifted slightly to the left and is in accord with expectation.

CONCLUSIONS

Rapid phase space density measurements were accomplished with relative ease, after the initial operation problems of the ion source testing facility were solved. The sensitivity of the apparatus is very good as demonstrated by the detection of the radial emittance asymmetry (Sec. 2.6).

The most important result of this series of studies was the measurement of the luminosity of H^+. The luminosity was found to be ten times larger than previously estimated. The implications of these results are that nuclear physicists should be able to do experiments at the optimum count rate with a better ultimate resolution than previously expected. Investigations of different chimney geometries (e.g., larger face angle, thinner chimney slit widths) may lead to additional improvement of the luminosity.

Space charge effects at the center of the cyclotron are a topic of current investigation. An interesting result of this research was the axial space charge effect (Sec. 2.5). The important result of these measurements was that increasing the chimney face angle in the axial direction results in an electric focusing force. This focusing may be used to counteract axial beam expansion due to space charge. In addition this apparatus may be used to verify some of the results predicted by the recently derived space charge equations[11].

Acceleration of H^- ions in a cyclotron is common today. It is known that the arc conditions for H^- ions are different

than for H^+ ions and one would expect that the chimney barrel diameter and face angle may affect the luminosity differently. Hence the studies of these effects should be carried out for H^- ions.

REFERENCES

1. B. L. Cohen, Rev. Sci. Instr. 33, 85 (1962).

2. R. L. Mills and A. M. Sessler, MURA Report #433 (1958).

3. A. van Steenbergen, IEEE Trans. on Nucl. Sci. NS-12, #3, 746 (June, 1965).

4. Th. Sluyters, CERN MPS/Int 1963, LIN 63-6.

5. H. G. Blosser and M. M. Gordon, Nucl. Instr. & Methods 13, 101 (1961).

6. W. I. B. Smith, Sector Focused Cyclotrons NAS-NRC pub 656, 183 (1959).

7. MSU Proposal for a Nuclear Reasearch Facility, Appendix C, Page 13 (June, 1961).

8. M. Reiser, Mich. State Univ. Cyclotron Report, MSUCP-16 (March, 1963).

9. R. S. Livingston and R. J. Jones, Rev. Sci. Instr. 25, 552 (1954).

10. K. R. MacKenzie, Nucl. Instr. & Methods 31, 139 (1964).

11. M. Reiser, private communication.